Composite Structures 278 (2021) 114695

Contents lists available at ScienceDirect

Composite Structures

journal homepage: www.elsevier.com/locate/compstruct

Analysis-oriented model for FRP confined high-strength concrete: 3D interpretation of path dependency

Jia-Qi Yang [a], Peng Feng [b,*]

[a] School of Mechanics and Civil Engineering, China University of Mining and Technology (Beijing), Beijing 100083, China
[b] MOE Key Laboratory of Civil Engineering Safety and Durability of China, Department of Civil Engineering, Tsinghua University, Beijing 100084, China

ARTICLE INFO

Keywords:
Path dependency
High-strength concrete
Confined concrete
Analysis-oriented model
FRP
LRS FRP

ABSTRACT

Various analysis-oriented models have been developed over the past decades to predict the stress-strain relationship of fibre-reinforced polymer (FRP) confined concrete. Most of these models are built based on the path-independent assumption, and the mechanism of this kind of model has been revealed by the authors based on a 3D geometrical approach. However, it is widely recognized that FRP confined high-strength concrete (HSC) is path dependent, which means that the stress of passively confined HSC deviates from the actively confined test results. Most of the existing solutions for this problem employ an alternative stress-strain relationship instead of the original actively confined HSC model for FRP confined HSC. In this paper, the mechanism of the path-dependency of confined HSC is revealed based on the 3D geometrical method. In addition, a corresponding analysis-oriented model for confined HSC considering path dependency is proposed. This model includes an actively confined concrete model, a damage criterion and post-damaged HSC behaviours. The proposed model can identify the confining mode from the load path and can select a proper stress-strain relationship for confined HSC without artificial intervention. Finally, the proposed model is calibrated and verified by test data collected from the literature. The results show that the proposed model has better accuracy than existing path-dependent models.

1. Introduction

The axial compressive strength and ductility of concrete can be significantly enhanced by the presence of lateral confining pressure. If the confining stress does not change with lateral expansion, the concrete is actively confined. Normal triaxial testing is a typical scenario of active confinement. In contrast, if the confining stress changes depending on the lateral expansion, it is classified as passively confined. Fibre-reinforced polymer (FRP) confined concrete is a typical scenario of passive confinement since the confining stress increases linearly with the lateral expansion during the axial compression process. The behaviours of FRP confined concrete have been investigated over the past decades, and various analytical models have been proposed by researchers worldwide [1]. These models can be classified into two major types: (a) design-oriented models and (b) analysis-oriented models. Path independency is the foundation of current analysis-oriented models, which means that for both actively and passively confined cases, concrete cylinders with the same lateral confining stress (σ_l) and axial compressive strain (ε_c) have the same axial stress (σ_c). With this assumption, analysis-oriented models can be built with an actively confined concrete model in conjunction with a model that predicts the lateral expansion of concrete. Yang and Feng [2] revealed the mechanism of analysis-oriented models using a 3D geometrical approach. This approach is briefly introduced as follows.

In the problem of uniformly confined concrete, the state of the concrete can be expressed by four variables: axial strain (ε_c), lateral strain (ε_l), axial stress (σ_c), and lateral confining stress (σ_l). The relationships for the four variables are interpreted geographically, as shown in Fig. 1a. First, the four axes of $\vec{\varepsilon_c}$, $\vec{\varepsilon_l}$, $\vec{\sigma_c}$ and $\vec{\sigma_l}$ are arranged in the 3D space. These four axes form two coordinate systems, i.e., the *axial stress coordinate system* (ε_c,σ_l,σ_c) and the *lateral strain coordinate system* (ε_l,σ_l,ε_c). The concrete state is a pair of points in the two coordinate systems, and the test results are the trace of the state points during the loading process. The ε_c-σ_l-σ_c relationship is governed by the actively confined concrete model (herein denoted as the *1st equation*), as shown by the red mesh in the axial stress coordinate system. Similarly, the equation governing the relationship of ε_l-σ_l-ε_c is denoted as the *2nd equation*, which is shown by the blue mesh in the lateral strain coordinate system. The relationship between ε_l and σ_l is denoted as the *3rd*

* Corresponding author.
E-mail addresses: yangjiaqi@cumtb.edu.cn (J.-Q. Yang), fengpeng@tsinghua.edu.cn (P. Feng).

https://doi.org/10.1016/j.compstruct.2021.114695
Received 17 June 2021; Received in revised form 5 September 2021; Accepted 11 September 2021
Available online 20 September 2021
0263-8223/

Nomenclature

A, B	Parameters of the factional stress-strain model of confined concrete
D	Diameter of the confined concrete cylinder
E_c	Elastic modulus of concrete
E_l	Confining stiffness
E_{frp}	Elastic modulus of FRP
f_{cc}^*	Axial compression strength of concrete with a confining stress of σ_l
$f_{cc}^{'}$	Maximum axial stress of FRP confined concrete
$f_{cc,a}^*$	Peak axial stress of actively confined concrete with a confining stress of σ_l
$f_{cc,d}^*$	f_{cc}^* of confined concrete at the damage initiation point
$f_{co}^{'}$	Compression strength of unconfined concrete
K_f, K_e	Reduction factor of the damaged 2nd equation functions
r	Parameter of Popovics' model
t_{frp}	Thickness of the FRP jacket
x	Normalized axial strain
y	Normalized axial stress
β	Reduction factor of σ_{act}
$\Delta\sigma_l$	Reduction in the lateral confining stress
ε_c	Axial strain of the confined concrete cylinder
ε_{cc}^*	Axial strain corresponding to f_{cc}^*
$\varepsilon_{cc,a}^*$	Axial strain corresponding to $f_{cc,a}^*$
$\varepsilon_{cc,d}^*$	$\varepsilon_{cc}^*$of confined concrete at the damage initiation point
ε_{co}	Axial strain corresponding to $f_{co}^{'}$
ε_{cu}	Ultimate axial strain of FRP confined concrete
ε_l	Lateral strain of the confined concrete cylinder
σ_{act}	Axial stress of the actively confined concrete
σ_{pas}	Axial stress of the passively confined concrete
σ_c	Axial stress of the confined concrete cylinder
σ_l	Lateral stress of the confined concrete cylinder
$\sigma_{l,d}$	$\sigma_l$of confined concrete at the damage initiation point

equation. If the concrete is actively confined, σ_l will be a constant value and does not change with ε_l, whereas if the concrete is passively confined, the 3rd equation depends on the properties of the confining material. If the path-independent assumption is valid, the pair of points must lie on the surfaces in corresponding coordinate systems, and as the loading process continues, the state points will change and leave two traces in the two coordinate systems. In fact, all types of curves for the test results are projections of the state traces on different planes, and the shapes of the result curves are controlled by the above mentioned three equations. Fig. 1b-d show the state traces and their projections of three typical confining modes. For actively confined concrete, as shown in Fig. 1b, the projections of the state traces on the ε_l-σ_l plane are straight lines parallel to the $\vec{\varepsilon_l}$ axis, which means that the confining stress does not change with lateral expansion. The axial stress–strain curves are the projections of the state traces on the ε_c-σ_c plane. If concrete is confined by linear elastic FRP (Fig. 1c), the 3rd equations are straight lines passing through the origin. The slopes of the lines of the 3rd equations denote the confining stiffness:

$$E_l = \frac{2E_{frp}t_{frp}}{D} \tag{1}$$

where E_l is the confining stiffness, E_{frp} is the elastic modulus of the FRP, t_{frp} is the thickness of the FRP jacket, and D is the diameter of the confined concrete cylinder. In this case, since the confining stress increases linearly with the lateral expansion, the projection of the state traces on the ε_c-σ_c plane can have a second ascending branch. Fig. 1d shows the case of concrete confined by steel without considering the steel buckling or biaxial bahaviour, such as steel tube confined concrete columns with load applied purely on the concrete, and steel spirals confined concrete cylinders. The ε_l-σ_l curve starts from the origin with a linear ascending portion before the steel yields, after which the confining stress remains constant and does not change with lateral expansion. Therefore, the behaviour of steel confined concrete is similar to that of concrete confined by linear FRP before the steel yielding point. When the confining steel yields, the axial stress–strain behaviour follows the scenario of active confinement. In summary, the 1st and 2nd equations are constitutive relationships of concrete, and the 3rd equation is the external constraint of the state path denoting the mechanical properties of the confining material. The generalized forms of the three equations are:

$$1^{st}\ \text{Equation}: \quad f(\varepsilon_c, \sigma_l, \sigma_c) = 0 \tag{2}$$

$$2^{nd}\ \text{Equation}: \quad g(\varepsilon_c, \sigma_l, \varepsilon_l) = 0 \tag{3}$$

$$3^{rd}\ \text{Equation}: \quad h(\varepsilon_l, \sigma_l) = 0 \tag{4}$$

By combining Eqs. (2)–(4), the state trace of confined concrete can be solved. According this theory, the authors developed a website program which can visually demonstrate the state path of confined concrete [3]. Users can select and combine the pre-defined or user defined 1st, 2nd and 3rd equations to predict the stress–strain behaviour of concrete under different confinement scenarios.

The path-independent assumption for normal strength concrete (NSC) has been confirmed by many researchers by comparing the collected test results of actively and passively confined concrete (e.g., Spoelstra and Monti [4], Teng et al. [5], Yang and Feng [2]). Furthermore, a direct evidence was provided by Lim and Ozbakkaloglu [6], in which cylinders sampled from the same batch of concrete were tested under active and FRP confinement. The results showed that for normal strength concrete, with the same ε_c and σ_l, both actively confined and FRP confined concrete cylinders exhibited very close values for σ_c and ε_l, respectively.

With the development of concrete technology, the application of high-strength concrete (HSC) has become popular in the construction industry, and novel structural members incorporating HSC have been developed by researchers to date [7–10]. Due to the brittle nature of HSC, the application of confinement is one of the optimum solutions for enhancing both strength and ductility. The triaxial strength and stress–strain behaviours of HSC have been investigated by many researchers based on normal triaxial tests [6,11–14]. However, when HSC is passively confined, the axial stress (σ_{pas}) is always lower than the actively confined axial stress (σ_{act}) with the same ε_c and σ_l, which indicates that the path-independent assumption is no longer applicable. Fig. 2 provides an intuitive illustration of this phenomenon. The results shown in Fig. 2 are obtained from Ref. [6]. All specimens were made from the same batch of HSC with an unconfined axial compressive

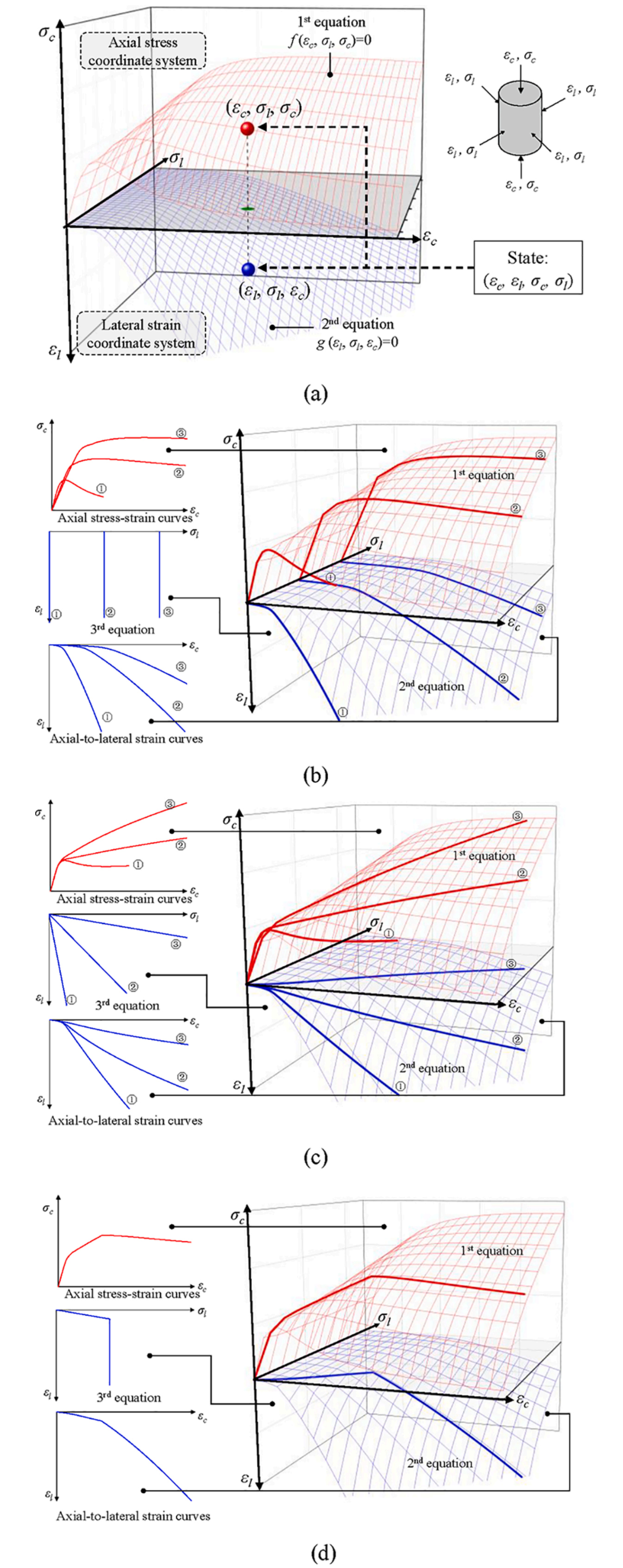

Fig. 1. 3D interpretation of analysis-oriented model for confined concrete [2]: (a) interpretation of the concrete state; (b) state paths for actively confined concrete; (c) state paths for linear elastic FRP confined concrete; and (d) state paths for steel confined concrete.

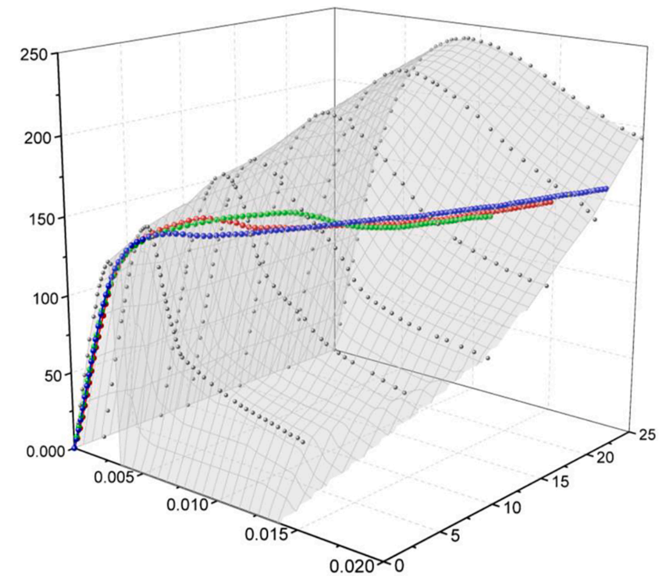

Fig. 2. Path dependency of passively confined HSC.

strength of $f_{co}^{'} = 128$ MPa. The grey dots represent the results from actively confined tests with σ_l ranging from 0 to 25 MPa, and the grey mesh is constructed by interpolating the discrete data points. The coloured dots represent the test results for specimens confined by two layers of aramid FRP (AFRP), carbon FRP (CFRP) or glass FRP (GFRP), respectively. Fig. 2 shows that after the initial ascending portion, the state traces of passively confined specimens lie below the grey mesh, thereby demonstrating the inapplicability of the path-dependent assumption.

Many researchers have made efforts to solve this problem by proposing new analysis-oriented models. The existing solutions can be classified into three types: (i) employing separate sets of parameters for the 1st equations for actively and passively confined cases (e.g., Xiao et al. [15], Ho et al. [16], Lai et al. [17]); (ii) introducing a reduction factor for the 1st equation depending on the current confining stress and/or confining stiffness (e.g., Chen et al. [18], Lai et al. [19]); and (iii) reducing the confining stress for FRP confined HSC (e.g., Lim and Ozbakkaloglu [20], Chin et al. [21], Lin et al. [22]). Typical examples for the three types of solutions are reviewed and demonstrated herein.

Xiao et al. [15] discussed the path dependency of HSC. Their solution was to provide the 1st equation parameters for "HSC" and "HSC&NSC" separately. The model framework was adopted from Jiang and Teng [23]. In the work of Ho et al. [16] and Lai et al. [17], two different sets of parameters for the 1st equations were proposed for actively confined concrete and FRP confined concrete. The parameters for FRP confinement are directly calibrated from the collected test results. The two 1st equations for Lai et al.'s [17] model are plotted in Fig. 3a. The grey mesh is the 1st equation for actively confined concrete (herein *active 1st equation*), and the coloured surface is the 1st equation for FRP confined concrete (herein *passive 1st equation*). The surface for the passive 1st equation lies below the active 1st equation surface, indicating that $\sigma_{pas} \leq \sigma_{act}$. It should be noted that Lai et al.'s [17] model does not distinguish between NSC and HSC.

Chen et al.'s [18] model is presented herein as an example for the type-ii models. Ref. [18] considers the path dependency by introducing a reduction factor β to the calculated actively confined axial stress; hence, $\sigma_{pas} = \beta\sigma_{act}$ and $\beta \leq 1$. In Ref. [18], σ_{act} is calculated by an analysis-oriented FRP confined concrete model that employs parameters selected from multiple studies, and σ_{pas} is calculated by the predictions of a design-oriented model proposed by Lim and Ozbakkaloglu [24]. The factor β is calibrated by the difference between the predictions of the two models. The expression for β is related to the lateral confining

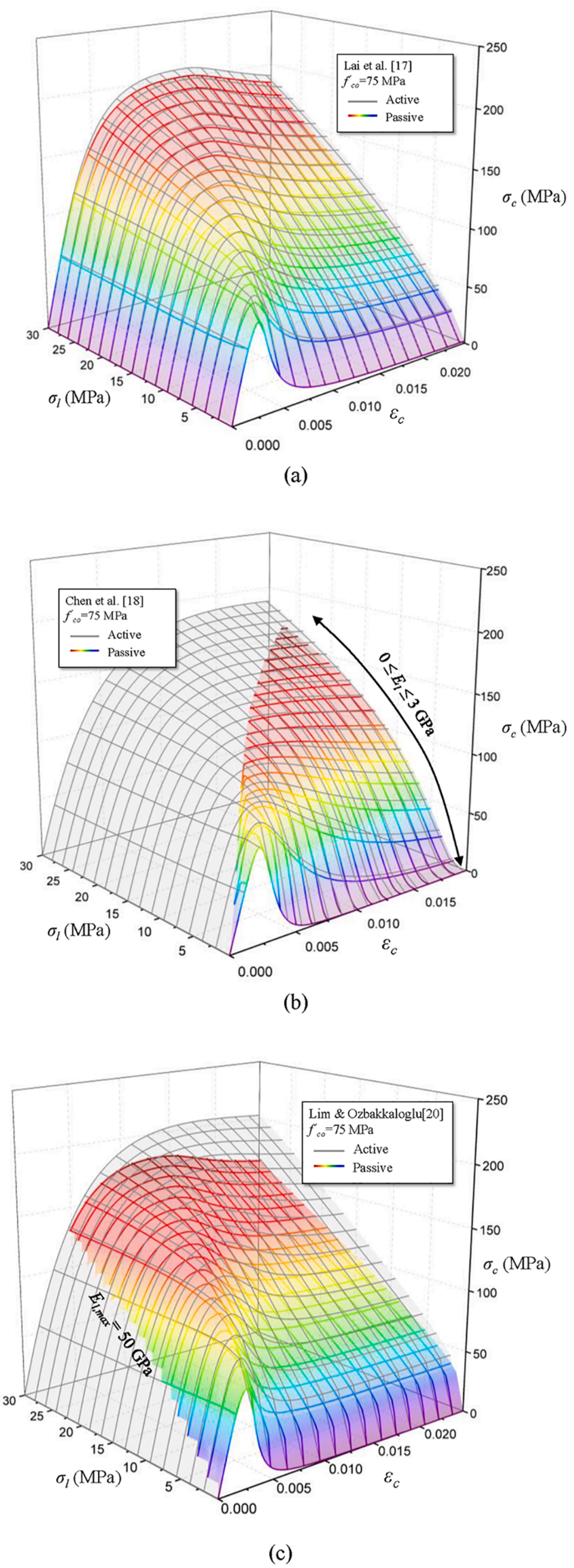

Fig. 3. 1st equations for typical path dependent models: (a) Lai et al.'s [17] model; (b) Chen et al.'s [18] model; (c) Lim and Ozbakkaloglu's [20] model.

stiffness E_l and confining stress σ_l. The effective range of Chen et al.'s [18] model is $0 \le E_l \le 3000$ MPa and 30 MPa $\le f_{co}^{'} \le 75$ MPa. Although different confining paths result in variations in β, the concrete state ε_c-σ_l-σ_c can still be expressed by a single surface, which is demonstrated in Fig. 3b. The coloured surface is the reduced 1st equation of actively confined concrete within the effective range of this model.

In the type-iii models, when using the 1st equation to calculate the axial stress of confined concrete (σ_c), the corresponding lateral confining stress (σ_l) is reduced according to E_l, σ_l or other factors related to the loading path. This method uses an active 1st equation with a reduced σ_l to calculate the σ_{pas}. This approach is an indirect way of reducing the 1st equation. The model proposed by Lim and Ozbakkaloglu [20] is demonstrated in Fig. 3c. In this model, the reduction in lateral confining stress $\Delta\sigma_l$ is related to E_l; therefore, the region near the σ_l axis has a singularity ($E_l \rightarrow +\infty$), and only part of the 1st equation with $0 \le E_l \le 50$ GPa is plotted.

The three examples shown in Fig. 3 have the same value of$f_{co}^{'} = 75$ MPa. The grey meshes for the three typical models are slightly different due to different parameters selected for the 1st equations. Nevertheless, all the three models demonstrate that the 1st equations for passive confinement are reduced from the active equations, which agrees with the basic finding that $\sigma_{pas} \le \sigma_{act}$. All the above mentioned models perform well with their own databases. However, these models still have some limitations. First, when these models are applied, the user should determine the confining mode first, i.e., active confinement or passive confinement. It is not applicable to incorporate this step into finite element analysis as a constitutive model for concrete [25,26]. In finite element analysis, the load or stress path of concrete may be complicated, and the user is not able to dictate whether a certain concrete element is passively or actively confined in each analysing step. Second, in some of the Type-ii and Type-iii models, the rules for reducing the 1st equation depend on E_l, which implies that E_l needs to be a constant value; hence, the model cannot be applied when E_l changes during the loading process, such as PEN or PET FRP confined concrete [27–29]. Third, as shown in Fig. 3b and 3c, although the reduction rules rely on E_l and σ_l, the 1st equation can still be interpreted with a single surface for a certain value of $f_{co}^{'}$. This means that once $f_{co}^{'}$ is determined, there is a unique solution for σ_c when ε_c and σ_l are known. Strictly speaking, these are not path-dependent models. Last, it should be noted that the value of $f_{co}^{'}$ for this demonstration is considering the validity range of Chen et al's [18] model. Since the active 1st equation surfaces (grey) are presented in the normalized coordinate system, they do not change much with $f_{co}^{'}$. The passive 1st equation surfaces (rainbowed) are reduced from the active ones. Since Lai et al. [17] provides a constant value of this factor, the passive surface does not change with $f_{co}^{'}$. When increasing the value of $f_{co}^{'}$, Chen et al.'s [18] model results in a higher reduction factor which makes the two surfaces closer, while Lim and Ozbakkaloglu's [20] model leads to an opposite result.

In the present study, the authors aim to develop analysis-oriented models for confined HSC considering path dependency. The proposed model has three basic characteristics: (i) it is capable of modelling confined HSC with arbitrary paths; (ii) it can identify the confining mode from the loading history and choose the proper subsequent 1st equation without artificial intervention; and (iii) it is a constitutive model for HSC and is independent of external conditions such as the confining stiffness. In this paper, the mechanism of the path dependency is interpreted by the 3D geometrical method. Then, the mathematical form of the analysis-oriented model is proposed, and the parameters of the model are calibrated with collected test data. Finally, the proposed model is validated based on a database of results for tests on FRP confinement as well as individual test results for large rupture strain (LRS) FRP confinement.

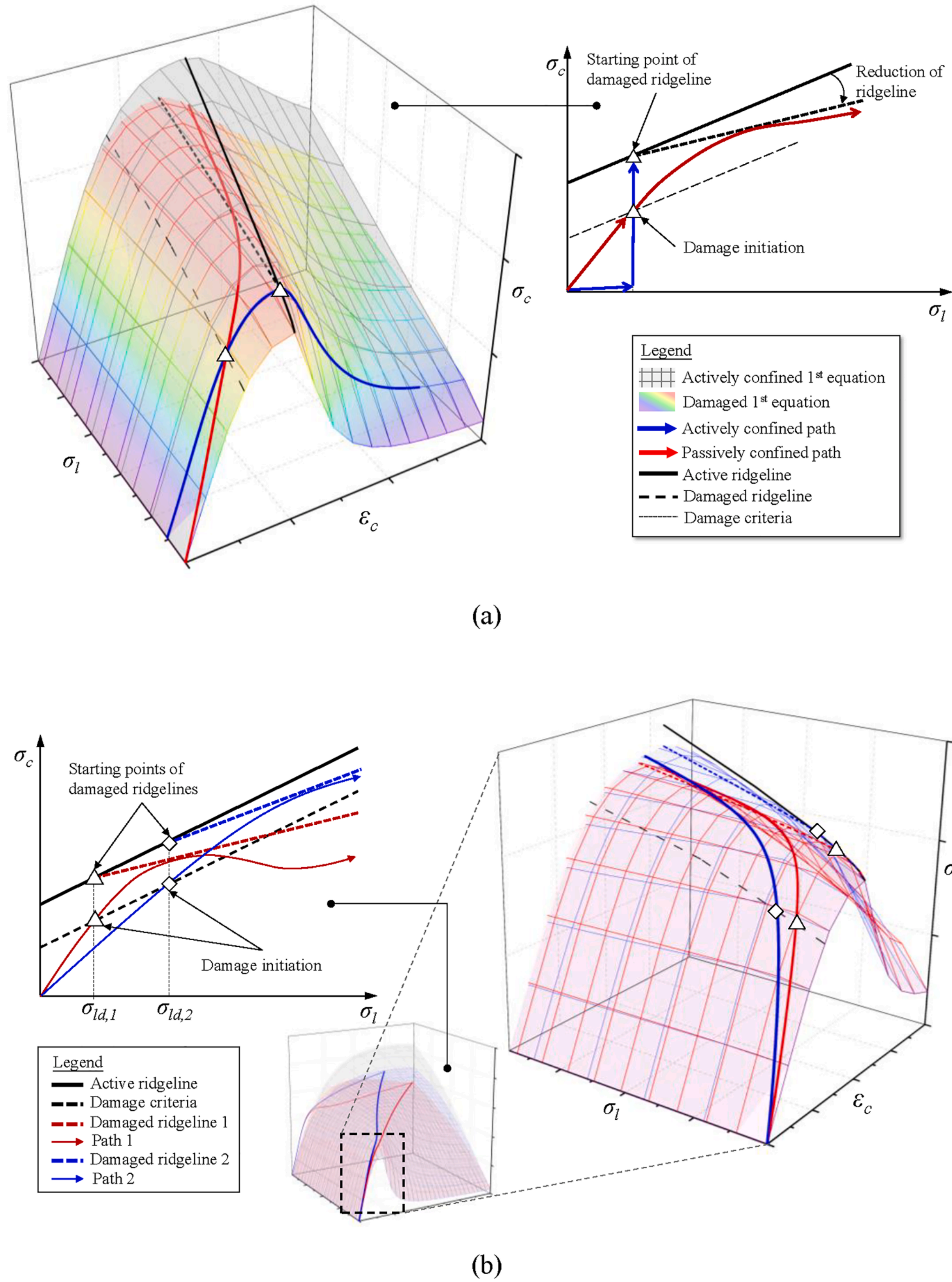

Fig. 4. 3D interpretation of the proposed model framework: (a) paths of actively and passively confined concrete; (b) paths of passively confined concrete with different confining stiffness.

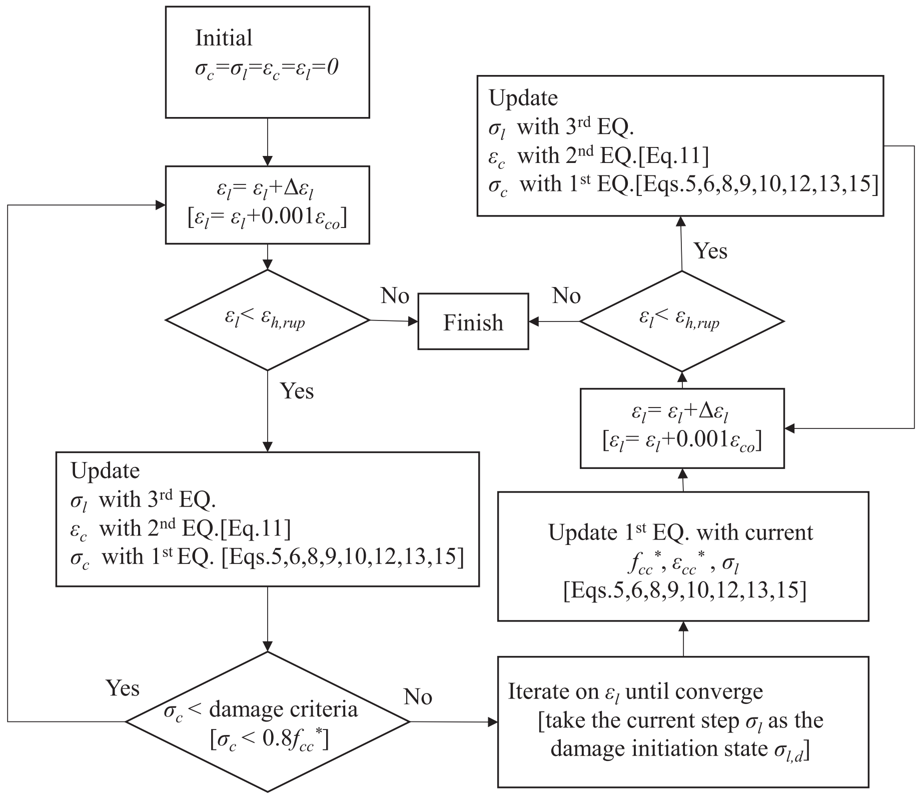

Note: the texts in the brackets [ ] denote the simplified approach using the proposed model

Fig. 5. Flow chart for path-dependent analysis-oriented model.

2. 3D interpretation of path dependency

There are three key issues for the proposed model: (i) the 1st equation for active confinement; (ii) damage initiation; and (iii) the reduction rules for the 1st equation of post-damaged concrete.

In normal triaxial tests, both lateral confining stress and axial compression stress are increased to the target level first. In this stage, the stress state develops along the hydrostatic axis, and no damage occurs in the concrete. Then, axial load is applied with a maintained lateral stress level. The loading path of the normal triaxial test postpones the damage more effectively than any other passive confinement; hence, there is $\sigma_{pas} \leq \sigma_{act}$, which explains the basic findings that the active 1st equation is the upper limit for passively confined concrete, and the behaviour of passively confined HSC is a reduction of the active 1st equation.

It is hypothesized by the authors that the path dependency of HSC is attributed to the initiation of internal cracks. For NSC, the strength of the mortar matrix is always lower than that of the coarse aggregates. Therefore, the cracks propagate within the matrix or in the transition zone between the matrix and aggregates. The cracked surface of NSC is coarse, and interlocking action will occur between the aggregates. Hence, the cracks are smeared inside the specimen. By contrast, the mortar matrix of HSC is stronger than the coarse aggregates, and the cracks may propagate through the aggregates. The cracked surface is relatively smooth compared with that of NSC. The confined HSC specimens usually fail with a few critical cracks and several discrete concrete blocks. Therefore, the directions of the initial cracks of HSC determine the crack propagation and mechanical behaviour for the subsequent loading stages. In the proposed model, the concrete state at the damage initiation point is recorded and used to calculate the subsequent mechanical behaviour.

In order to model the phenomenon that $\sigma_{pas} \leq \sigma_{act}$, the 1st equation needs to be reduced from the active 1st equation after damage initiation. As discussed by Yang and Feng [2], all points of (f_{cc}^*, σ_l, ε_{cc}^*) form the ridgeline of the surface of the 1st equation, where f_{cc}^* is the axial compression strength of concrete with a confining stress of σ_l, and ε_{cc}^* is the corresponding axial strain. The shape of the 1st equation surface can be manipulated by adjusting the ridgeline functions. In the proposed model, the reduction rules are applied on the ridgeline functions after damage initiation. Besides, the active and post-damaged 1st equation surfaces should be consecutive in the axial stress coordinate system to prevent singularities. In addition, as found by Lim and Ozbakkaloglu [6], the 2nd equation for confined HSC is path independent, which means that regardless of whether it is actively or passively confined, the points (ε_l, σ_l, ε_c) always lie on the same spatial surface. Therefore, there is no need to adjust the 2nd equation for different loading paths.

With the three key issues discussed above, the mechanism of the proposed model is shown schematically in Fig. 4. The analysing procedures are listed below, and the flowchart for generalized methodology is shown in Fig. 5:

Step 1: Choose a proper active 1st equation and 2nd equation to build an analysis-oriented model following the methodology proposed by Yang and Feng [2];

Table 1
Database of actively confined HSC.

Source	ID	$f_{co}^{'}$ (Mpa)	ε_{co}	σ_l (Mpa)	f_{cc}^{*} (Mpa)	ε_{cc}^{*}	$f_{cc}^{*}/f_{co}^{'}$	$\varepsilon_{co}/\varepsilon_{cc}^{*}$	$\sigma_l/f_{co}^{'}$
Xie and Elwi[2] [11]	A0	60.4	0.0026	0.0	60.4	0.0030	1.00	1.13	0.00
	A1	60.2	0.0026	2.3	80.6	0.0055	1.34	2.11	0.04
	A2	60.2	0.0026	5.3	97.6	0.0074	1.62	2.83	0.09
	A3	60.2	0.0026	8.3	107.6	0.0093	1.79	3.56	0.14
	A4	60.2	0.0026	0.0	68.3	0.0038	1.14	1.47	0.00
	A5	60.2	0.0026	20.3	156.9	0.0212	2.61	8.12	0.34
	A6	60.2	0.0026	29.3	193.3	0.0227	3.21	8.69	0.49
	A7	60.2	0.0026	23.3	172.1	0.0208	2.86	7.98	0.39
	A8	60.2	0.0026	11.3	121.6	0.0115	2.02	4.42	0.19
	A9	60.2	0.0026	14.3	136.8	0.0141	2.27	5.38	0.24
	A10	60.2	0.0026	0.8	58.4	0.0064	0.97	2.46	0.01
	A11	60.2	0.0026	0.0	64.4	N/A[1]	1.07	1.00	0.00
	B0	93.0	0.0029	0.0	93.0	0.0032	1.01	1.00	0.00
	B1	92.2	0.0029	3.8	129.4	0.0060	1.40	2.05	0.04
	B2	92.2	0.0029	8.3	155.6	0.0080	1.69	2.74	0.09
	B3	92.2	0.0029	12.8	181.2	0.0102	1.97	3.51	0.14
	B4	92.2	0.0029	17.3	194.3	N/A[1]	2.11	N/A[1]	0.19
	B5	92.2	0.0029	21.9	208.8	0.0127	2.26	4.36	0.24
	B6	92.2	0.0029	26.3	234.7	0.0154	2.55	5.31	0.29
	B7	92.2	0.0029	16.5	199.8	0.0115	2.17	3.96	0.18
	B8	92.2	0.0029	35.5	261.1	0.0237	2.83	8.16	0.39
	B9	92.2	0.0029	44.4	293.5	0.0243	3.18	8.38	0.48
	B10	92.2	0.0029	0.0	96.5	N/A[1]	1.05	1.00	0.00
	B11	92.2	0.0029	0.0	86.9	N/A[1]	0.94	1.00	0.00
	C0	119.8	0.0031	0.0	119.8	0.0037	0.98	1.18	0.00
	C1	122.3	0.0031	6.2	177.1	0.0065	1.45	2.08	0.05
	C2	122.3	0.0031	12.4	218.1	0.0077	1.78	2.46	0.10
	C3	122.3	0.0031	18.5	232.2	0.0104	1.90	3.33	0.15
	C4	122.3	0.0031	24.7	258.0	0.0112	2.11	3.61	0.20
	C5	122.3	0.0031	30.8	269.1	0.0133	2.20	4.25	0.25
	C6	122.3	0.0031	37.1	288.8	0.0134	2.36	4.30	0.30
	C7	122.3	0.0031	49.3	325.2	0.0179	2.66	5.76	0.40
	C8	122.3	0.0031	61.7	377.6	0.0249	3.09	7.98	0.50
	C9	122.3	0.0031	0.0	100.4	N/A[1]	0.82	1.00	0.00
	C10	122.3	0.0031	0.0	101.0	N/A[1]	0.83	1.00	0.00
	C11	122.3	0.0031	0.0	118.1	0.0038	0.97	1.23	0.00
Lim and Togay [6]	H128-T0-1	128.0	0.0032	0.0	127.0	0.0032	0.99	1.02	0.00
	H128-T0-2	128.0	0.0032	0.0	128.9	0.0031	1.01	0.98	0.00
	H128-T2.5–1	128.0	0.0032	2.5	139.7	0.0035	1.09	1.11	0.02
	H128-T2.5–2	128.0	0.0032	2.5	146.5	0.0036	1.14	1.14	0.02
	H128-T5-1	128.0	0.0032	5.0	156.2	0.0040	1.22	1.27	0.04
	H128-T5-2	128.0	0.0032	5.0	156.1	0.0041	1.22	1.30	0.04
	H128-T7.5–1	128.0	0.0032	7.5	172.0	0.0049	1.34	1.56	0.06
	H128-T7.5–2	128.0	0.0032	7.5	175.0	0.0050	1.37	1.59	0.06
	H128-T10-1	128.0	0.0032	10.0	179.1	0.0054	1.40	1.71	0.08
	H128-T10-2	128.0	0.0032	10.0	181.9	0.0052	1.42	1.65	0.08
	H128-T15-1	128.0	0.0032	15.0	203.1	0.0068	1.59	2.16	0.12
	H128-T15-2	128.0	0.0032	15.0	199.1	0.0065	1.56	2.06	0.12
	H128-T20-1	128.0	0.0032	20.0	227.5	0.0079	1.78	2.51	0.16
	H128-T20-2	128.0	0.0032	20.0	225.1	0.0083	1.76	2.63	0.16
	H128-T25-1	128.0	0.0032	25.0	244.2	0.0095	1.91	3.02	0.20
	H128-T25-2	128.0	0.0032	25.0	241.4	0.0093	1.89	2.95	0.20
Lu and Hsu [14]	U	67.0	0.0025	0.0	67.0	0.0025	1.00	1.00	0.00
	T1-3.5	67.0	0.0025	3.5	84.9	0.0045	1.27	1.77	0.05
	T1-7	67.0	0.0025	7.0	99.0	0.0078	1.48	3.09	0.10
	T1-14	67.0	0.0025	14.0	130.7	0.0124	1.95	4.92	0.21
	T2-14	67.0	0.0025	14.0	134.4	0.0132	2.01	5.26	0.21
	T1-21	67.0	0.0025	21.0	154.0	0.0166	2.30	6.61	0.31
	T2-21	67.0	0.0025	21.0	159.2	0.0188	2.38	7.50	0.31
	T1-28	67.0	0.0025	28.0	180.2	0.0250	2.69	9.95	0.42
	T2-28	67.0	0.0025	28.0	179.9	0.0241	2.69	9.58	0.42
	T1-42	67.0	0.0025	42.0	229.1	0.0321	3.42	12.78	0.63
	T1-56	67.0	0.0025	56.0	276.0	0.0406	4.12	16.14	0.84
Ansari and Li [12]	HS10-0	71.1	0.0020	0.0	71.1	0.0020	1.00	1.00	0.00
	HS10-1	71.1	0.0020	13.2	129.1	0.0080	1.82	3.94	0.19
	HS10-2	71.1	0.0020	26.3	156.1	0.0126	2.20	6.21	0.37
	HS10-3	71.1	0.0020	39.5	185.4	0.0204	2.61	10.08	0.56
	HS10-4	71.1	0.0020	52.6	209.4	0.0302	2.95	14.90	0.74
	HS10-5	71.1	0.0020	65.8	224.8	0.0387	3.16	19.09	0.93
	HS15-0	107.3	0.0019	0.0	107.3	0.0019	1.00	1.00	0.00
	HS15-1	107.3	0.0019	20.9	192.5	0.0089	1.79	4.60	0.19
	HS15-2	107.3	0.0019	41.8	233.0	0.0106	2.17	5.50	0.39
	HS15-3	107.3	0.0019	62.7	285.9	0.0193	2.67	9.97	0.58
	HS15-4	107.3	0.0019	83.6	314.9	0.0210	2.94	10.83	0.78

(continued on next page)

Table 1 (*continued*)

Source	ID	f'_{co} (Mpa)	ε_{co}	σ_l (Mpa)	f^*_{cc} (Mpa)	ε^*_{cc}	f^*_{cc}/f'_{co}	$\varepsilon_{co}/\varepsilon^*_{cc}$	σ_l/f'_{co}
Candappa et al. [2] [13]	U60-0	60.6	0.0026	0.0	60.6	N/A[1]	1.00	1.00	0.00
	U60-4	60.6	0.0026	4.0	78.3	0.0037	1.29	1.42	0.07
	U60-8	60.6	0.0026	8.0	97.7	0.0094	1.61	3.60	0.13
	U60-12	60.6	0.0026	12.0	115.1	0.0120	1.90	4.58	0.20
	U75-0	73.1	0.0027	0.0	73.1	N/A[1]	1.00	1.00	0.00
	U75-4	73.1	0.0027	4.0	102.5	0.0044	1.40	1.62	0.05
	U75-8	73.1	0.0027	8.0	121.1	0.0062	1.66	2.25	0.11
	U75-12	73.1	0.0027	12.0	137.5	0.0089	1.88	3.25	0.16
	U100-0	103.3	0.0030	0.0	103.3	N/A[1]	1.00	1.00	0.00
	U100-4	103.3	0.0030	4.0	132.4	0.0038	1.28	1.28	0.04
	U100-8	103.3	0.0030	8.0	157.1	0.0058	1.52	1.93	0.08
	U100-12	103.3	0.0030	12.0	171.1	0.0070	1.66	2.34	0.12

Notes:

[1] N/A = unable to obtain from the reference. It is assumed that $\varepsilon_{co}/\varepsilon^*_{cc} = 1$ when $\sigma_l = 0$, otherwise it is excluded for data analysis

[2] Xie and Elwi [11] and Candappa et al. [13]: ε_{co} is not provided, hence it is calculated as $\varepsilon_{co} = 0.000937(f'_{co})^{0.25}$ [30]

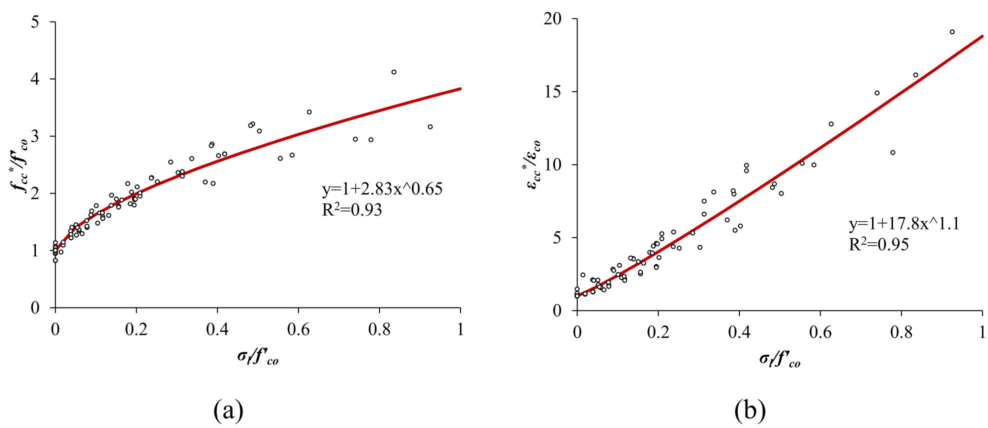

Fig. 6. Calibration of the ridgeline functions: (a) normalized axial strength versus confining stress; (b) normalized axial strain versus confining stress.

Step 2: Set a damage criterion for the confined HSC;

Step 3: Start the incremental analysis until the concrete state reaches the damage criterion, and record the corresponding values for σ_l, f^*_{cc} and ε^*_{cc} at the damage initiation point as ($f^*_{cc,d}, \sigma_{l,d}, \varepsilon^*_{cc,d}$);

Step 4: Adjust the subsequent ridgeline from the point ($f^*_{cc,d}, \sigma_{l,d}, \varepsilon^*_{cc,d}$) following certain reduction rules and update the 1st equation for the post-damaged HSC;

Step 5: Continue the incremental analysis using the updated 1st equation.

An example of actively and passively confined HSC is demonstrated in Fig. 4a. The grey mesh represents the active 1st equation, and the light black dashed curve represents the damage criterion. The state traces of actively and passively confined HSC are presented by blue and red curves, respectively. Before damage ($\sigma_l \le \sigma_{l,d}$), the concrete state traces lie on the grey mesh. When the state traces reach the damage criterion, a new ridgeline bifurcates from the original ridgeline at point ($f^*_{cc,d}$, $\sigma_{l,d}$, $\varepsilon^*_{cc,d}$), and a reduced 1st equation surface is then formed for the damaged HSC, which is shown by the coloured surface in Fig. 4a. The coloured surface and the grey mesh coincide before damage ($\sigma_l \le \sigma_{l,d}$) and bifurcate from $\sigma_l = \sigma_{l,d}$. As can be observed in the present example, the state path of actively confined HSC still follows the active 1st equation, while the state path of passively confined HSC follows an updated 1st equation when $\sigma_l > \sigma_{l,d}$. Based on this method, $\sigma_{pas} \le \sigma_{act}$ can be modelled with a unified expression, and there is no need to choose different 1st equations for different confining modes in the beginning of the analysis.

An example of passively confined HSC with different confining stiffnesses is shown in Fig. 4b. The red curve is the state path for a lower confining stiffness (Path 1), and the blue curve is the state path for a higher confining stiffness (Path 2). The red and blue meshes in the 3D plot represent the damaged 1st equations for these two cases. Since the confining stiffness for Path 2 is higher than that of Path 1, the blue curve enters the damaged stage with a higher $\sigma_{l,d}$; hence, the ridgelines for these two cases bifurcate from the active ridgeline at different locations and can have different reduction rules. This agrees with the basic findings that both the confining stiffness and confining stress can influence the reduction in the active 1st equation [6,18] and enables more flexibility in the calibration of the model parameters.

3. Details of the proposed model

3.1. 1st equation

A total of 85 tests are collected from Xie et al. [11], Ansari and Li [12], Candappa et al. [13], Lu and Hsu [14] and Lim and Ozbakkaloglu [6] for the calibration of the active 1st equation. The f'_{co} for the collected data ranges from 60 MPa to 128 MPa, and the σ_l applied during the tests

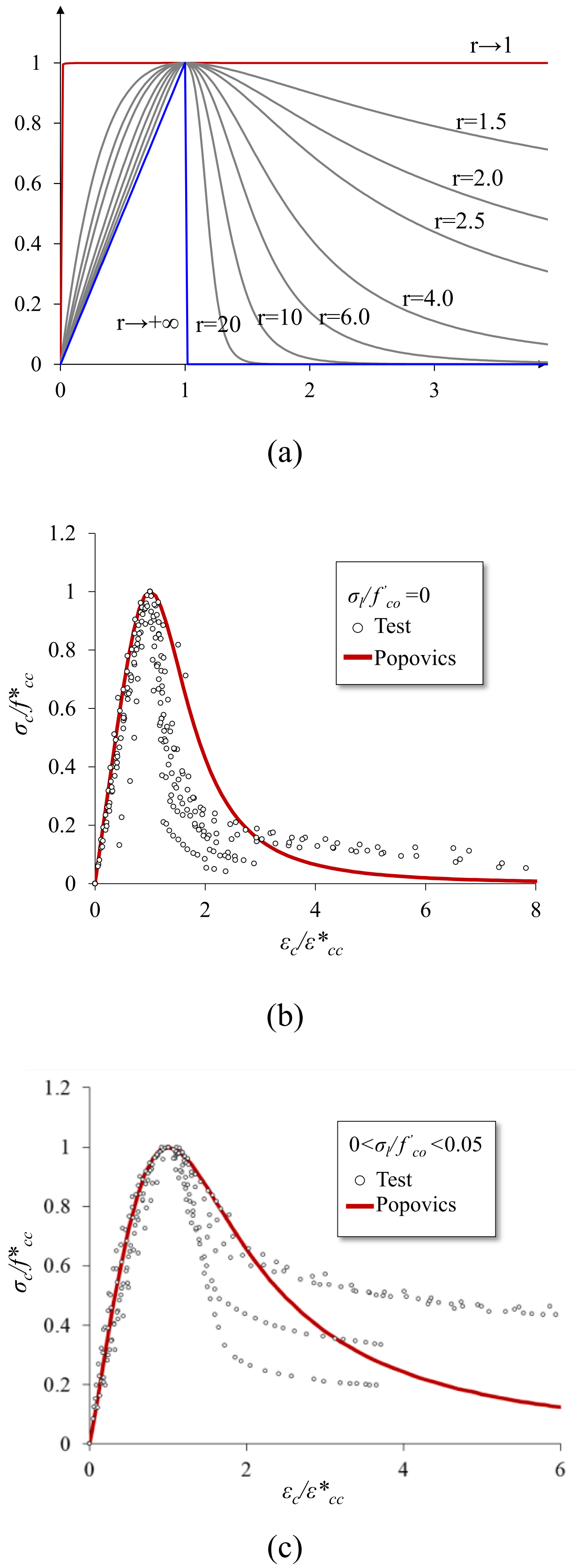

Fig. 7. Limitation of Popovics' model: (a) Influence of factor 'r'; (b) Performance of Popovics' model for unconfined HSC; (c) Performance of Popovics' model for lower confining stress.

is between 0 and 83.6 MPa. The collected test data are listed in Table 1. The ridgelines are calibrated in the form of a power function as:

$$\frac{f^*_{cc,a}}{f'_{co}} = 1 + 2.83\left(\frac{\sigma_l}{f'_{co}}\right)^{0.65} \tag{5}$$

$$\frac{\varepsilon^*_{cc,a}}{\varepsilon_{co}} = 1 + 17.8\left(\frac{\sigma_l}{f'_{co}}\right)^{1.1} \tag{6}$$

$f^*_{cc,a}$ is the peak axial stress of actively confined concrete with a confining stress of σ_l, and $\varepsilon^*_{cc,a}$ is the corresponding axial strain. Both factors are positive for compression. ε_{co} is the axial strain corresponding to the peak axial stress for unconfined concrete and can be calculated by $\varepsilon_{co} = 0.000937(f'_{co})^{0.25}$ [30]. The performances of Eq. (1) and Eq. (2) are shown in Fig. 6a and 6b, respectively. The two equations fit the test data well with goodness of fit (R^2) of 0.93 and 0.95, respectively.

In general, the curve of the normalized active 1st equation exhibits an ascending branch and a descending branch with a peak point (1,1). As reviewed by Ref. [1], Popovics' [30] model is widely adopted for the 1st equation in existing analysis-oriented models for FRP confined concrete, and it was also adopted by Xiao et al. [15] and Chen et al. [18] to model HSC. The generalized form of Popovics' formula is:

$$y = \frac{x \cdot r}{r - 1 + x^r} \tag{7}$$

where x and y are the normalized axial strain and stress, respectively. The factor r controls both the initial stiffness and the shape of the post peak descending branch of the curve. As shown in Fig. 7a, with the increase of r, the initial stiffness decreases and approaches 1.0, and the post-peak branch becomes steeper. However, Popovics' model is not able to capture the characteristics of HSC, especially when the confining stress is low. For unconfined HSC, the brittleness results in sudden failure, and there is a very steep or almost vertical descending branch. With the presence of confining stress, the confined HSC experiences a quick loss of strength after reaching the peak load, followed by a residual plateau. The data points obtained from the test curves in the database (Table 1) are normalized by f^*_{cc} and ε^*_{cc} and are plotted in Fig. 7b and 7c. This method of normalization excludes the influence of concrete strength and solely exhibits the curve shape. As shown in Fig. 7b, Popovics' curve cannot capture the brittle failure of HSC, and Fig. 7c indicates that Popovics' curve is not able to simulate the residual plateau.

The fractional equation (Eq. (8)) is an alternative option to model the axial stress–strain behaviour of concrete.

$$y = \frac{Ax + (B-1)x^2}{1 + (A-2)x + Bx^2} \tag{8}$$

where $x = \frac{\varepsilon_c}{\varepsilon^*_{cc}}$ and $y = \frac{\sigma_c}{f^*_{cc}}$. This equation has the following characteristics: (i) $y(0) = 0$ and $y(1) = 1$; (ii) $y'(0) = A$ and $y'(1) = 0$; and (iii) $y(+\infty) = \frac{1-B}{B}$. When A > 1 and B > 1, the curve has a convex ascending branch and concave descending branch joining at the peak point of (1,1). Parameters A and B control the initial slope and residual plateau of the curve, which is flexible for model calibration. Early study can be found in Sargin [31]. Based on this equation, Attard and Setunge [32] proposed an actively confined concrete model with complex parameters, which has been adopted by researchers to model FRP confined concrete (e.g., [17,19,33]). For simplicity, the parameters A and B are proposed by the authors:

$$A = \begin{cases} \dfrac{E_c}{f^*_{cc}/\varepsilon^*_{cc}} & \text{when } \varepsilon_c \le \varepsilon^*_{cc} \\ \dfrac{E_c}{f^*_{cc}/\varepsilon^*_{cc}}\left(0.24\left(\dfrac{\sigma_l}{f'_{co}}\right)^{0.25} + 0.01\right) & \text{when } \varepsilon_c \le \varepsilon^*_{cc} \end{cases} \tag{9}$$

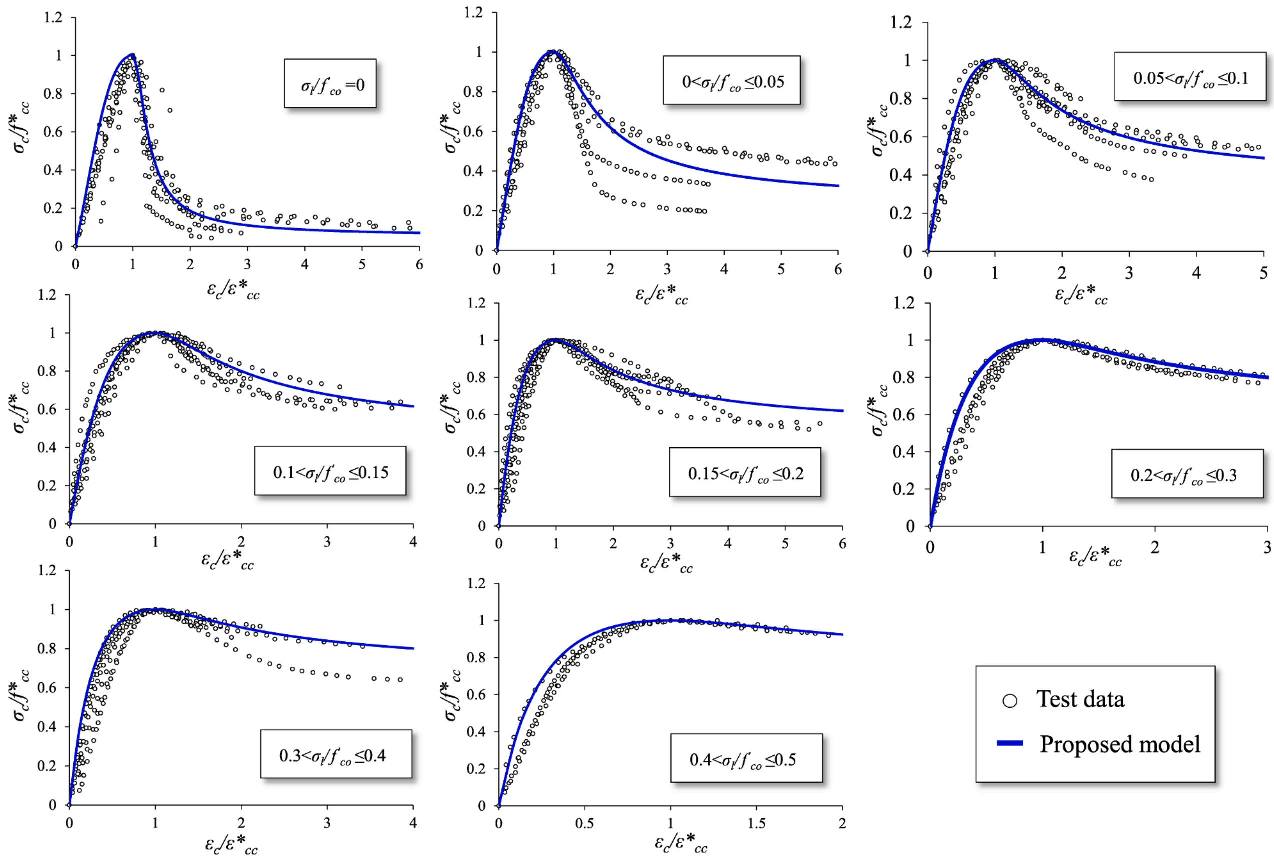

Fig. 8. Performance of the proposed 1st equation.

Table 2
Database for model calibration.

Source	ID	$f_{co}^{'}$ (MPa)	ε_{co}	E_c (MPa)	E_{frp} (MPa)	t_{frp} (mm)	D (mm)
Xiao et al. [15]	F70.8-1ply	70.8	0.0032	39,900	237,800	0.340	152
	F70.8-3ply	70.8	0.0032	39,900	237,800	1.020	152
	F70.8-5ply	70.8	0.0032	39,900	237,800	1.700	152
	F111.6-2ply	111.6	0.0034	46,400	237,800	0.680	152
	F111.6-3ply	111.6	0.0034	46,400	237,800	1.020	152
	F111.6-5ply	111.6	0.0034	46,400	237,800	1.700	152
Lim and Ozbakkaloglu [6]	H128-A2-2	128.0	0.0031	49,780	128,500	0.400	63
	H128-C2-1	128.0	0.0031	49,780	236,000	0.222	63
	H128-G2-2	128.0	0.0031	49,780	95,300	0.400	63
Dang et al. [34]	N-G-2	79.7	0.0025	35,700	91,100	0.338	100
	N-G-5	79.7	0.0025	35,700	91,100	0.845	100
	N-G-8	79.7	0.0025	35,700	91,100	1.352	100
	N-C-2	79.7	0.0025	35,700	236,900	0.338	100
	N-C-5	79.7	0.0025	35,700	236,900	0.845	100
	N-C-8	79.7	0.0025	35,700	236,900	1.352	100

$$B = 5\left(\frac{\sigma_l}{f_{co}^{'}}\right) + 1.05 \tag{10}$$

where E_c is the elastic modulus of concrete and can be calculated by $E_c = 4730\sqrt{f_{co}^{'}}$ [5]. The performance of the proposed model is shown in Fig. 8. The test data obtained from the database (Table 1) are normalized by f_{cc}^{*} and ε_{cc}^{*}. It should be noted that the normal triaxial test results of HSC have considerable variation in the descending branch, and there is no obvious trend for the influence of $f_{co}^{'}$. Different testing equipment may lead to different results. It is difficult to propose a model that fits each test curve well, but it is important to reflect the basic behaviour and trend of the test results. As shown in Fig. 8, the proposed model is able to simulate the behaviours of confined HSC at different levels of confining stress.

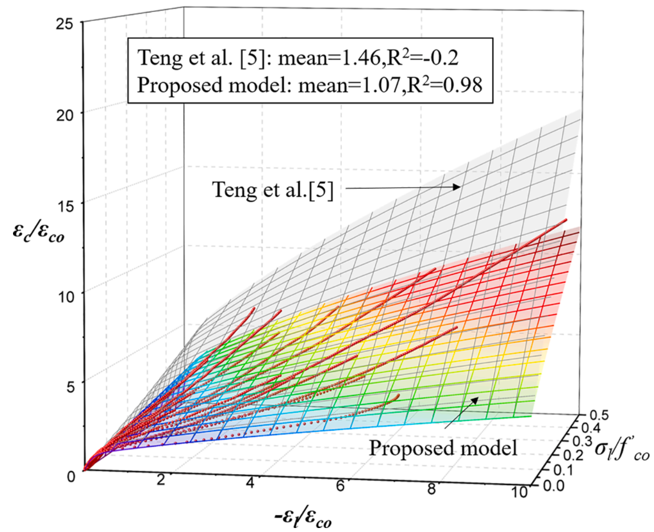

Fig. 9. Calibration of the 2nd equation.

3.2. 2nd equation

A test database for calibrating the FRP confined HSC model is established, as presented in Table 2. The 18 test specimens are collected from Refs. [6,15,34] because: (1) both ε_c-σ_c and ε_l-σ_l relationships are reported; (2) the results clearly exhibit the bilinear response without premature failure, and the post-transition behaviour is fully developed. The datapoints of (ε_l, σ_l, σ_c) are used to calibrate the 2nd equation. Finally, the Teng et al.'s [5] 2nd equation is modified to:

$$\frac{\varepsilon_c}{\varepsilon_{co}} = 0.85\left\{\left[1+0.75\left(-\frac{\varepsilon_l}{\varepsilon_{co}}\right)\right]^{0.7} - \exp\left[-7\left(-\frac{\varepsilon_l}{\varepsilon_{co}}\right)\right]\right\}\left[1+3.9\left(\frac{\sigma_l}{f'_{co}}\right)^{0.9}\right] \tag{11}$$

It should be noted that ε_l is negative for tensile strain. As shown in Fig. 9, the Teng et al.'s [5] model overestimates the axial strain (ε_c) by an average prediction-to-test ratio of 1.46. The proposed model has a mean value of 1.07 and $R^2 = 0.98$ for the data points shown in the figure.

3.3. Damage criterion

As discussed earlier, the path dependency of confined HSC arises from the formation of internal cracks. According Dong et al. [35], for both actively and passively confined concrete, the transition point on the ε_l-ε_c curve represents the formation of internal cracks. When cracks form, the lateral expansion of the concrete accelerates, and the confined concrete changes from an elastic isotropic material to an inelastic anisotropic material. The transition point always occurs prior to the peak axial stress. By analysing 95 passively confined and 34 actively confined test results, Dong et al. [35] concluded the formation of internal cracks occurs when the axial stress reaches $0.8f^*_{cc}$. This conclusion is adopted in this study. Therefore, when projected on the σ_l-σ_c plane, the damage criterion is parallel to the ridgeline, which is schematically shown in Fig. 4a and 4b.

3.4. Reduction rules for post-damaged 1st equation

As can be observed from the test database, the difference between σ_{pas} and σ_{act} is smaller with higher confining stress and confining stiffness. This phenomenon is confirmed by Chen et al. [18] and Lim and Ozbakkaloglu [20] that these two factors are involved in their models. According to the theory of this study, higher confining stress and confining stiffness postpone the specimens entering the damaged status. Therefore, if the specimen reaches the damage criteria early (i.e., with a smaller $\sigma_{l,d}$), there needs to be more reduction for the subsequent 1st equation. On the contrary, if the specimen enters the damaged status with a higher $\sigma_{l,d}$, the 1st equation shall be less reduced. Following this inference, the mathematical expression for the ridgeline functions considering path dependency are proposed by the author as following:

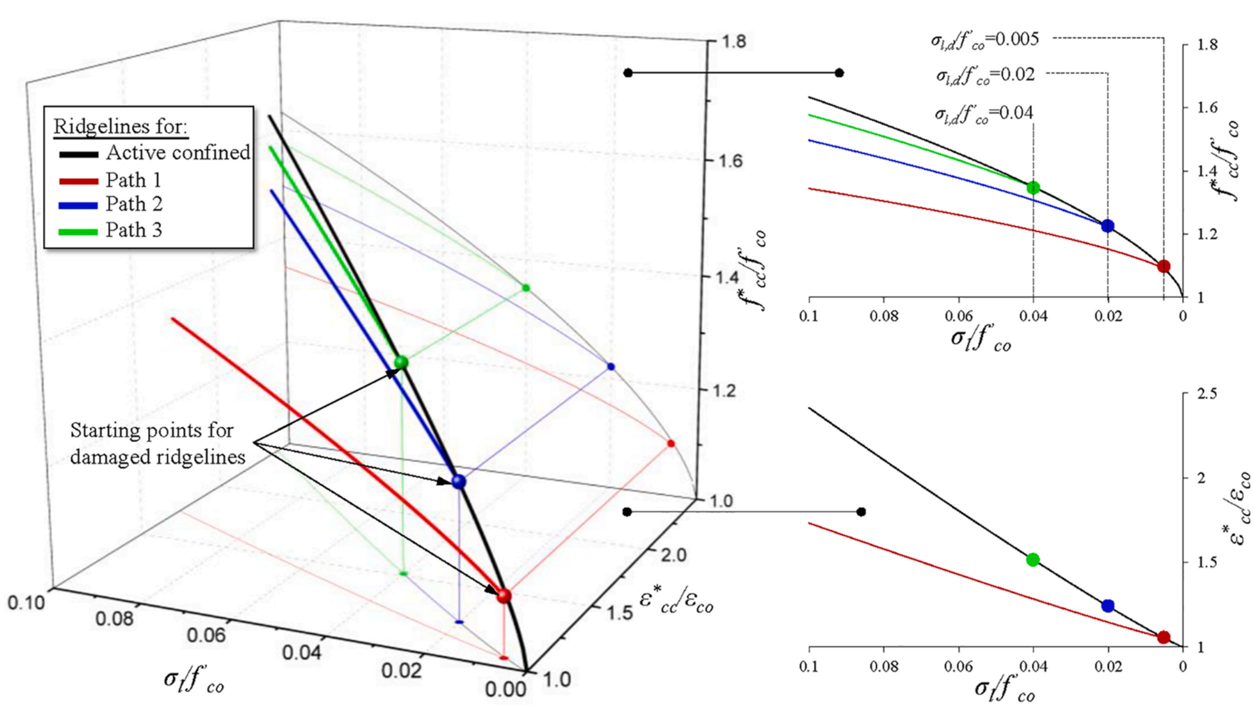

Fig. 10. Reduction in the damaged ridgeline.

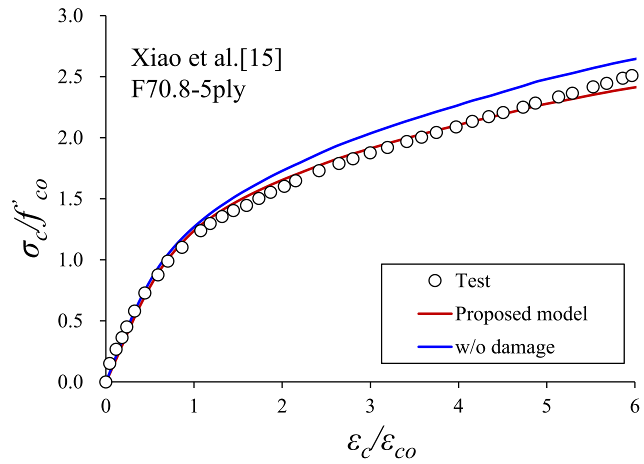

(a)

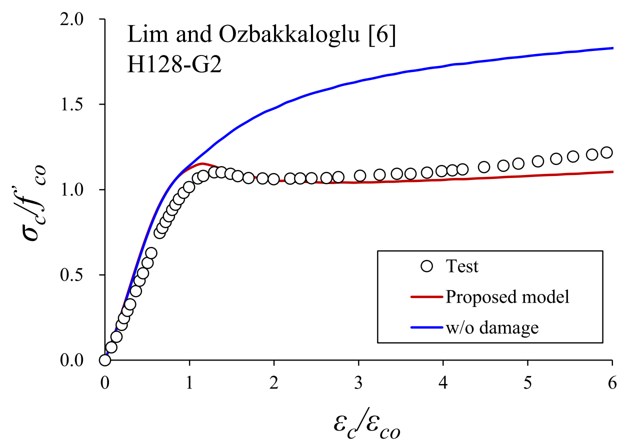

(b)

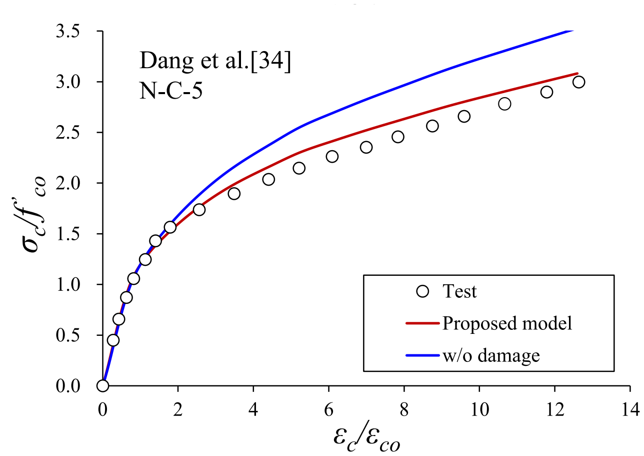

(c)

Fig. 11. Performance of the proposed model for individual test results: (a) Specimen F70.8-5ply [15]; (b) Specimen H128-G2-2 [6]; and (c) Specimen N-C-5 [34].

$$f^*_{cc} = \begin{cases} f^*_{cc,a} & when\ \sigma_l \le \sigma_{l,d} \\ K_f f^*_{cc,a} + (1-K_f) f^*_{cc,d} & when\ \sigma_l > \sigma_{l,d} \end{cases} \tag{12}$$

$$\varepsilon^*_{cc} = \begin{cases} \varepsilon^*_{cc,a} & \text{when } \sigma_l \le \sigma_{l,d} \\ K_e \varepsilon^*_{cc,a} + (1-K_e) \varepsilon^*_{cc,d} & \text{when } \sigma_l > \sigma_{l,d} \end{cases} \tag{13}$$

K_f and K_e are reduction factors. $f^*_{cc,a}$ and $\varepsilon^*_{cc,a}$ can be calculated by Eqs. (5) and (6). It should be noted that f^*_{cc} and $f^*_{cc,a}$ are functions of σ_l, and $f^*_{cc,d}$, $\varepsilon^*_{cc,d}$ and $\sigma_{l,d}$ are fixed values determined following the method presented in section 2. A trial-and-error method is used to best fit the test data of the specimens listed in Table 2. K_f and K_e can be determined using the following equations:

$$K_f = \begin{cases} 0.4 + \dfrac{40\sigma_{l,d}}{3f'_{co}} & when\ \sigma_{l,d} \le 0.03f'_{co} \\ 0.8 & when\ \sigma_{l,d} > 0.03f'_{co} \end{cases} \tag{14}$$

$$K_e = \begin{cases} 100\dfrac{\sigma_{l,d}}{f'_{co}} & when\ \sigma_{l,d} \le 0.01f'_{co} \\ 1 & when\ \sigma_{l,d} > 0.01f'_{co} \end{cases} \tag{15}$$

Fig. 10 shows ridgelines for three different paths with $\sigma_l/f'_{co} = 0.005$, 0.02 and 0.04. When $\sigma_{l,d} \le 0.01f'_{co}$, both f^*_{cc} and ε^*_{cc} are reduced from the active ridgeline. When $\sigma_{l,d} \le 0.03f'_{co}$, with a higher value of $\sigma_{l,d}$, f^*_{cc} is less reduced. If $\sigma_{l,d} > 0.03f'_{co}$, the reduction ratio of f^*_{cc} is maintained at 0.8.

The prediction of the proposed model is compared with selected test data and plotted in Fig. 11. The model predictions without considering damage, which means keeping $f^*_{cc} = f^*_{cc,a}$ and $\varepsilon^*_{cc} = \varepsilon^*_{cc,a}$ for any σ_l, are also plotted in the figures with blue curves. The bifurcation point of the blue and red curves is located at $\sigma_l = \sigma_{l,d}$. As shown in Fig. 11, the confined HSC with different confining stiffnesses behave differently after the damage point, which agrees with the general findings from the test results. It should be noted that when applying the trial-and-error method to calibrate K_f and K_e, the lateral expansion of HSC is obtained from the test data.

In summary, Eqs. (5), (6), (8), (9), (10), (11), (12), (13), (14) and (15) form an analysis-oriented model for confined HSC incorporated with path dependency. The 1st equation (Eq. (2)) is expressed by Eqs. (5), (6), (8), (9), (10), (12), (13), (14) and (15), and the 2nd equation (Eq. (3)) is presented by Eq. (11). The 3rd equation depends on the properties of the confining material and specimen geometry. The problems of both actively and passively confined HSC can be solved based on the method proposed by Yang and Feng [2]. The most important step in this analysis is to solve for $\sigma_{l,d}$, which can be solved iteratively. In addition, if the increment of lateral strain is sufficiently small, for example, $\Delta\varepsilon_l = 1 \times 10^{-3}\varepsilon_{co}$, the result for $\sigma_{l,d}$ can be obtained by linear interpolation with sufficient accuracy. Readers can follow the flow chart presented in Fig. 5 to apply the proposed model with a simplified approach.

4. Model evaluation

The database established for model evaluation contains 143 test results collected from Refs. [36–38] because each of the selected research conducted large number of tests with systematically investigated parameters, thus the data is more reliable. The test results are listed in Table 3. In this database, f'_{co} ranges from 50 MPa to 149 MPa, the diameters of the tested cylinders are 50, 74, 100 and 152 mm. The confinement ratio $\rho_k = E_l/(\frac{f_{co}}{\varepsilon_{co}})$ is a dimensionless parameter representing the confining stiffness [2], which ranges from 0.005 to 0.162. f'_{cc} is chosen as the target result for comparison, which is the maximum axial

Table 3
Database for model evaluation.

Source	ID	f'_{co}(MPa)	D (mm)	E_{frp}(MPa or N/mm/ply)	t_{frp}(mm or ply)	$\varepsilon_{cu}/\varepsilon_{co}$	f'_{cc}/f'_{co}
Cui and Sheikh [36]	M1C1A	79.9	152	84,900	1	2.18	1.19
	M1C1B	79.9	152	84,900	1	3.07	1.32
	M1C2A	79.9	152	84,900	2	5.19	1.78
	M1C2B	79.9	152	84,900	2	4.04	1.76
	M1C3A	79.9	152	84,900	3	6.14	2.16
	M1C3B	79.9	152	84,900	3	6.12	2.28
	H1C1A	110.6	152	84,900	1	1.98	1.33
	H1C1B	110.6	152	84,900	1	2.10	1.35
	H1C3A	110.6	152	84,900	3	3.22	1.79
	H1C3B	110.6	152	84,900	3	2.79	1.65
	M1G1A	79.9	152	26,840	1	3.15	1.07
	M1G1B	79.9	152	26,840	1	3.64	1.11
	M1G2A	79.9	152	26,840	2	3.58	1.16
	M1G2B	79.9	152	26,840	2	3.22	1.18
	M1G3A	79.9	152	26,840	3	5.21	1.51
	M1G3B	79.9	152	26,840	3	4.90	1.58
	H1G2A	110.6	152	26,840	2	2.54	1.30
	H1G2B	110.6	152	26,840	2	1.75	1.30
	H1G4A	110.6	152	26,840	4	3.62	1.58
	H1G4B	110.6	152	26,840	4	4.89	1.56
	M2ST1A	85.6	152	26,821	1	1.72	1.11
	M2ST1B	85.6	152	26,821	1	1.69	1.05
	M2ST2A	85.6	152	26,821	2	2.17	1.12
	M2ST2B	85.6	152	26,821	2	2.26	1.10
	M2ST4A	85.6	152	26,821	4	3.86	1.46
	M2ST4B	85.6	152	26,821	4	3.84	1.48
	H2ST2A	111.8	152	26,821	2	1.24	1.20
	H2ST2B	111.8	152	26,821	2	1.84	1.21
	H2ST5A	111.8	152	26,821	5	1.90	1.36
	H2ST5B	111.8	152	26,821	5	2.22	1.37
	M2HM1A	85.6	152	71,316	1	1.63	1.13
	M2HM1B	85.6	152	71,316	1	2.10	1.16
	M2HM2A	85.6	152	71,316	2	2.74	1.38
	M2HM2B	85.6	152	71,316	2	2.14	1.37
	M2HM4A	85.6	152	71,316	4	3.94	1.89
	M2HM4B	85.6	152	71,316	4	3.69	1.90
	H2HM2A	111.8	152	71,316	2	1.24	1.36
	H2HM2B	111.8	152	71,316	2	1.20	1.33
	H2HM5A	111.8	152	71,316	5	1.87	1.64
	H2HM5B	111.8	152	71,316	5	1.91	1.59
Oliveira et al. [37]	HSC-1a	112	100	40,504	1	2.07	1.12
	HSC-1b	112	100	40,504	1	2.96	1.18
	HSC-3a	112	50	40,504	2	7.04	2.08
	HSC-3b	112	50	40,504	2	5.93	1.78
	HSC-4a	112	100	40,504	2	3.68	1.29
	HSC-4b	112	100	40,504	2	3.39	1.30
	HSC-5a	112	50	40,504	4	10.18	2.82
	HSC-5b	112	50	40,504	4	9.43	2.48
	HSC-6a	112	100	10,322	1	1.82	0.95
	HSC-6b	112	100	10,322	1	1.82	1.12
	HSC-7a	112	50	10,322	2	4.29	1.19
	HSC-7b	112	50	10,322	2	4.00	1.07
	HSC-8a	112	50	10,322	4	6.04	1.40
	HSC-8b	112	50	10,322	4	5.96	1.41
	HSC-SF1-1a	149	50	40,504	1	3.44	1.22
	HSC-SF1-1b	149	50	40,504	1	3.44	1.22
	HSC-SF1-2a	149	100	40,504	1	2.56	1.09
	HSC-SF1-2b	149	100	40,504	1	1.94	1.04
	HSC-SF1-3a	149	50	40,504	2	5.24	1.49
	HSC-SF1-3b	149	50	40,504	2	4.88	1.56
	HSC-SF1-4a	149	50	40,504	4	6.44	2.05
	HSC-SF1-4b	149	50	40,504	4	7.41	2.00
	HSC-SF1-5a	149	100	10,322	1	1.06	1.06
	HSC-SF1-5b	149	100	10,322	1	1.06	1.06
	HSC-SF1-6a	149	50	10,322	2	3.65	1.05
	HSC-SF1-6b	149	50	10,322	2	3.65	1.03
	HSC-SF1-7a	149	50	10,322	4	4.79	1.35
	HSC-SF1-7b	149	50	10,322	4	4.44	1.30
	HSC-SF2-1a	126	50	40,504	1	4.38	1.59
	HSC-SF2-1b	126	50	40,504	1	4.17	1.53
	HSC-SF2-2a	126	100	40,504	1	2.79	1.04
	HSC-SF2-2b	126	100	40,504	1	2.07	1.13
	HSC-SF2-3a	126	50	40,504	2	6.31	1.75
	HSC-SF2-3b	126	50	40,504	2	6.28	1.60

(continued on next page)

Table 3 (*continued*)

Source	ID	f'_{co}(MPa)	D (mm)	E_{frp}(MPa or N/mm/ply)	t_{frp}(mm or ply)	$\varepsilon_{cu}/\varepsilon_{co}$	f'_{cc}/f'_{co}
	HSC-SF2-4a	126	50	40,504	4	8.07	2.39
	HSC-SF2-4b	126	50	40,504	4	8.52	2.55
	HSC-SF2-5a	126	100	10,322	1	3.17	1.12
	HSC-SF2-5b	126	100	10,322	1	1.76	1.00
	HSC-SF2-6a	126	50	10,322	2	4.69	1.32
	HSC-SF2-6b	126	50	10,322	2	4.52	1.26
	HSC-SF2-7a	126	50	10,322	4	5.62	1.56
	HSC-SF2-7b	126	50	10,322	4	5.86	1.52
Togay and Vincent [38]	H1-75C1L-1	62	74	251,000	0.117	2.42	1.13
	H1-75C1L-2	66.6	74	251,000	0.117	2.11	1.07
	H1-75C1L-3	55	74	251,000	0.117	3.20	1.13
	H1-75C2L-1	55	74	251,000	0.234	5.72	1.75
	H1-75C2L-2	50.3	74	251,000	0.234	7.13	1.95
	H1-75C2L-3	52	74	251,000	0.234	10.04	2.03
	H1-100A2L-1	85.9	100	125,700	0.4	5.32	1.41
	H1-100A2L-2	82.4	100	125,700	0.4	5.10	1.30
	H1-100A2L-3	82.4	100	125,700	0.4	5.32	1.36
	H1-100A3L-1	85.9	100	125,700	0.6	6.19	1.73
	H1-100A3L-2	85.9	100	125,700	0.6	7.19	1.80
	H1-100A3L-3	85.9	100	125,700	0.6	7.68	1.86
	H1-100AFW0.6-1	85.9	100	125,700	0.6	9.32	2.05
	H1-100AFW0.6-2	83	100	125,700	0.6	8.16	1.87
	H1-100AFW0.6-3	85.9	100	125,700	0.6	9.32	2.09
	H1-150A3L-1	79.6	152	125,700	0.6	5.57	1.32
	H1-150A3L-2	77.2	152	125,700	0.6	5.47	1.32
	H1-150A3L-3	77	152	125,700	0.6	7.43	1.53
	H1-150C1L-1	59	152	251,000	0.117	2.77	1.00
	H1-150C1L-2	59	152	251,000	0.117	2.15	1.02
	H1-150C2L-1	59	152	251,000	0.234	3.65	1.16
	H1-150C2L-2	59	152	251,000	0.234	4.04	1.11
	H1-150C2L-3	62	152	251,000	0.234	3.23	1.08
	H1-150C3L-1	59	152	251,000	0.351	4.77	1.34
	H1-150C3L-2	65	152	251,000	0.351	4.81	1.20
	H1-150C3L-3	59	152	251,000	0.351	5.92	1.38
	H1-150HM1L-1	59	152	657,000	0.19	1.92	1.19
	H1-150HM1L-2	55.6	152	657,000	0.19	2.00	1.20
	H1-150HM1L-3	59	152	657,000	0.19	1.81	1.18
	H1-150HM2L-1	59	152	657,000	0.38	1.81	1.20
	H1-150HM2L-2	59	152	657,000	0.38	1.73	1.31
	H1-150HM2L-3	59	152	657,000	0.38	1.54	1.25
	H2-75C1L-1	75	74	251,000	0.117	2.28	1.15
	H2-75C1L-2	77	74	251,000	0.117	2.60	1.08
	H2-75C1L-3	83.1	74	251,000	0.117	2.26	1.02
	H2-75C2L-1	83.1	74	251,000	0.234	4.23	1.26
	H2-75C2L-2	83.1	74	251,000	0.234	3.74	1.34
	H2-75C3L-1	93.8	74	251,000	0.351	3.91	1.51
	H2-75C3L-2	99.9	74	251,000	0.351	3.71	1.21
	H2-75C3L-3	77	74	251,000	0.351	3.80	1.71
	H2-75C3L-4	82.5	74	251,000	0.351	3.13	1.49
	H2-100A3L-1	110.1	100	125,700	0.6	6.03	1.41
	H2-100A3L-2	110.1	100	125,700	0.6	4.89	1.37
	H2-100A3L-3	110.1	100	125,700	0.6	5.34	1.42
	H2-100A4L-1	110.1	100	125,700	0.8	6.31	1.67
	H2-100A4L-2	110.1	100	125,700	0.8	7.06	1.73
	H2-100AFW0.9-1	110.1	100	125,700	0.9	9.20	2.11
	H2-100AFW0.9-2	110.1	100	125,700	0.9	8.03	2.04
	H2-100AFW0.9-3	110.1	100	125,700	0.9	9.94	2.22
	H2-150A6L-1	104.5	152	125,700	1.2	5.82	1.57
	H2-150A6L-2	104.5	152	125,700	1.2	6.41	1.61
	H2-150A6L-3	104.5	152	125,700	1.2	6.03	1.71
	H2-150C3L-1	92.7	152	251,000	0.351	2.53	1.09
	H2-150C3L-2	94.7	152	251,000	0.351	2.70	1.10
	H2-150C3L-3	90.1	152	251,000	0.351	2.56	1.07
	H2-150C4L-1	93	152	251,000	0.468	2.79	1.05
	H2-150C4L-2	100	152	251,000	0.468	2.82	1.08
	H2-150C4L-3	97.5	152	251,000	0.468	3.06	1.10
	H2-150C6L-1	102.5	152	251,000	0.702	3.74	1.28
	H2-150C6L-2	96	152	251,000	0.702	3.52	1.29
	H2-150C6L-3	93	152	251,000	0.702	3.30	1.21

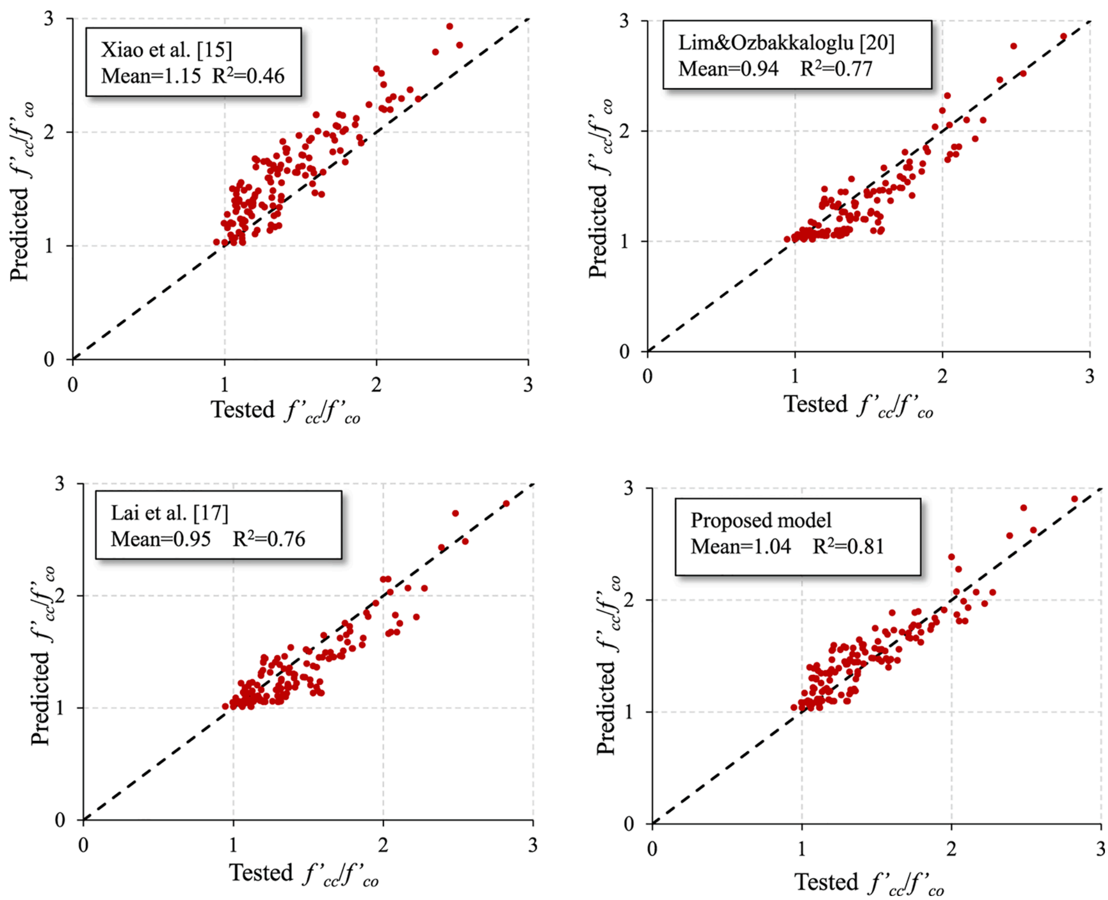

Fig. 12. Evaluation of the proposed model.

stress achieved by the specimen before reaching the ultimate axial strain (ε_{cu}). The performance of the proposed model is compared with the predictions of Xiao et al. [15], Lim and Ozbakkaloglu [20] and Lai et al. [17]. The results are shown in Fig. 12. Xiao et al.'s [15] model overestimates the test results by approximately 15% on average. Lai et al.'s [17] and Lim and Ozbakkaloglu's [20] models yield similar results in predicting f'_{cc}. The average prediction-to-test ratios are 0.95 and 0.94, and the R^2 values are 0.76 and 0.77 for Lai et al.'s [17] and Lim and Ozbakkaloglu's [20] models, respectively. The influence of the test parameters on the prediction/test ratio are plotted in Fig. 13. It can be observed from the figures that Xiao et al.'s [15] model overestimates the test results for most cases, and there is no obvious trend for the rest three models with respect to the test parameters. Although Lai et al.'s [17] and Lim and Ozbakkaloglu's [20] models adopt different approaches to address the path dependency, both of the two models exhibit good accuracy when modelling HSC. The proposed model achieves an average prediction-to-test ratio of 1.04 and R^2 of 0.81, which further improves the model performance and hence confirms the validity of the proposed theoretical framework and parameters.

Theoretically, the proposed model can predict the behaviour of confined HSC with arbitrary confining paths. Different from those models using the confining stiffness (E_l) to calculate the reductions of the 1st equation [18,20], this model employs the concrete state at the damage initiation point as the path indicator. Hence, the proposed model is applicable for the cases in which the confining stiffness changes during the loading process. A typical example of passive confinement with a nonconstant confining stiffness is that concrete confined by large rupture strain (LRS) FRP [29], such as PEN/PET FRP. The LRS FRP usually exhibits a bilinear stress–strain response when subjected to uniaxial tension, which results in two-stage behaviour of the confining stiffness [27,28]. The performance of the proposed model when predicting the stress–strain behaviour of LRS FRP confined HSC is shown in Fig. 14. The test results are obtained from Zeng et al. [39]. The analysed specimens are C2-P3-1 and C3-P3-1, with an unconfined HSC strength of 79.7 MPa and 114.9 MPa, respectively. Both specimens are confined with prefabricated FRP tubes made of 3 layers of PET fibre sheets. The PET FRP has an initial elastic modulus of 18.9 GPa and a second-stage modulus of 7.3 GPa. The contribution of FRP tubes is deducted from the tested axial stress–strain curves. The predictions of Xiao et al.'s [15] model are also plotted for comparison. Fig. 14 shows that both models have two turning points on the stress–strain curves, demonstrating the bilinear behaviour of the confining material. Xiao et al.'s [15] model overestimates the axial stress, although its database covers the HSC strength grades of the test specimens. The low initial confining stiffness provided by PET FRP (E_l = 329 MPa) results in early damage initiation of confined HSC. This is captured by the proposed model. As shown in Fig. 14, the result of the proposed model bifurcates from Xiao et al.'s [15] prediction near the first turning point of the stress–strain curve, which is close to the first peaks of the test data. This phenomenon indirectly verifies the hypothesis of this study and the framework of the proposed model. The bifurcation point represents the damage initiation inside the HSC, after which the proposed model employs a reduced 1st

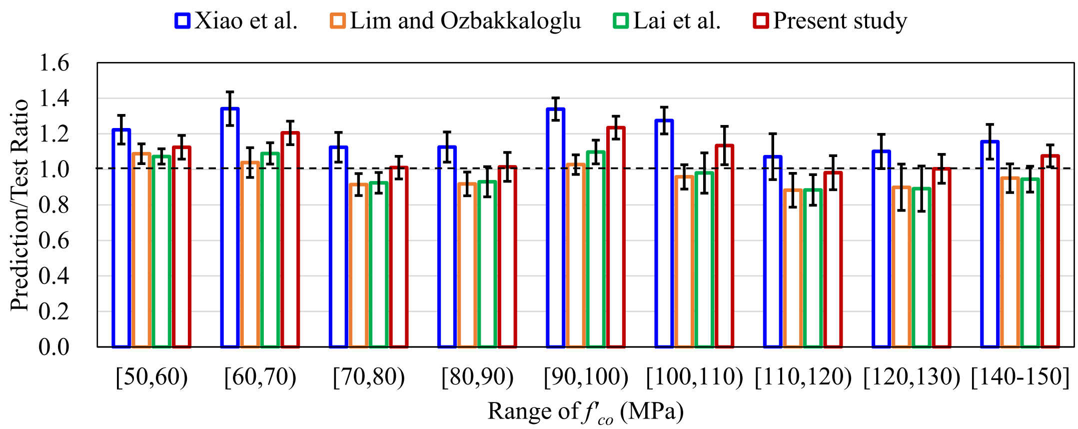

(a)

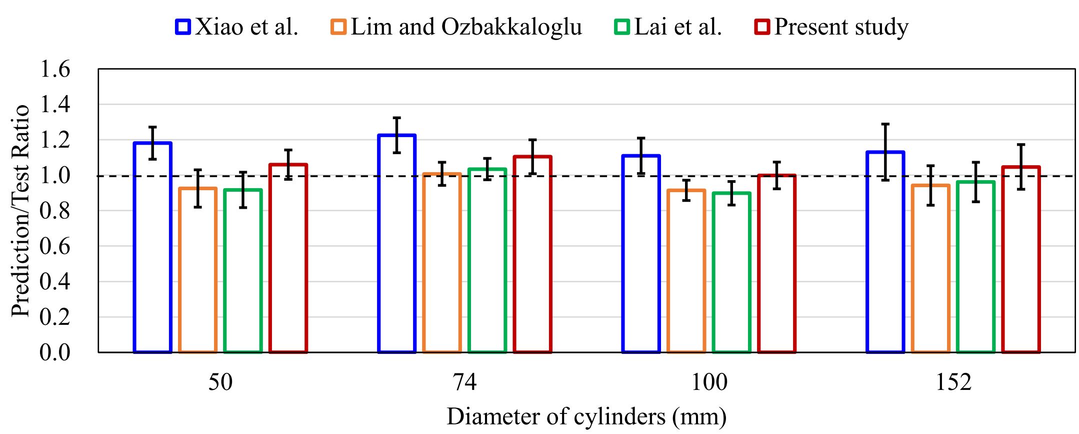

(b)

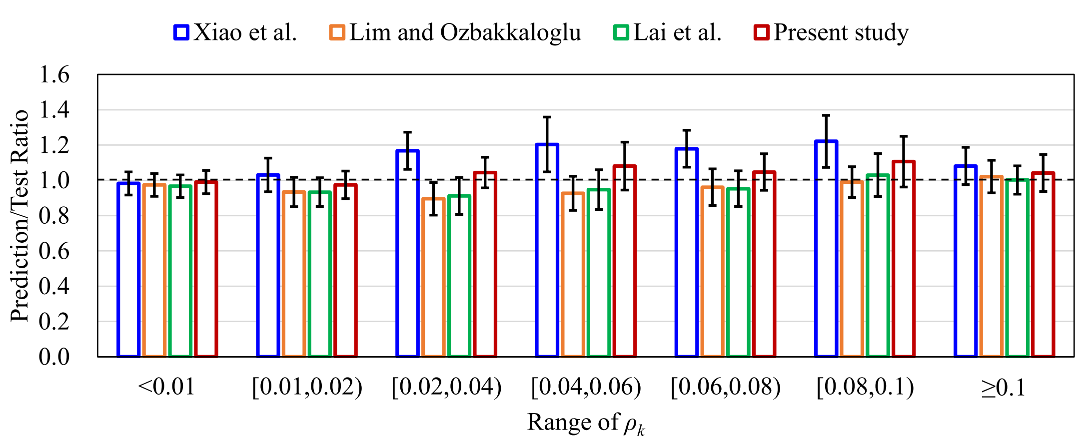

(c)

Fig. 13. Influence of test parameters on the prediction/test ratios: (a) influence of f'_{co}; (2) influence of diameters; (3) influence of confinement ratio.

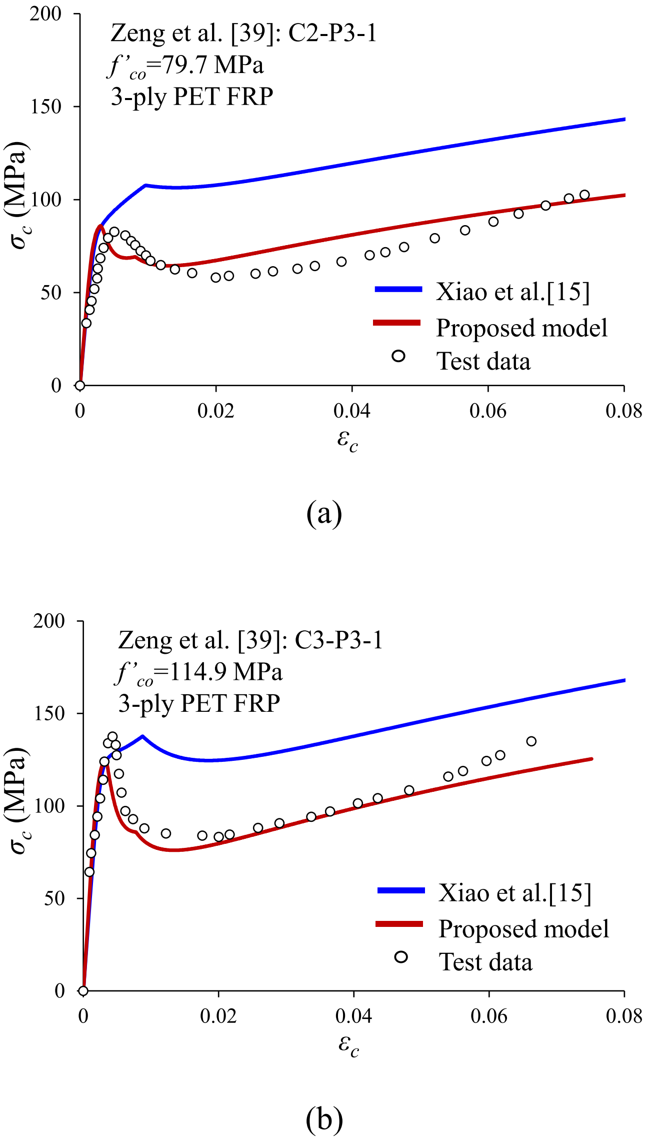

Fig. 14. Stress–strain behaviour of PET FRP confined HSC: (a) specimen C2-P3-1 [39]; (b) specimen C3-P3-1 [39]

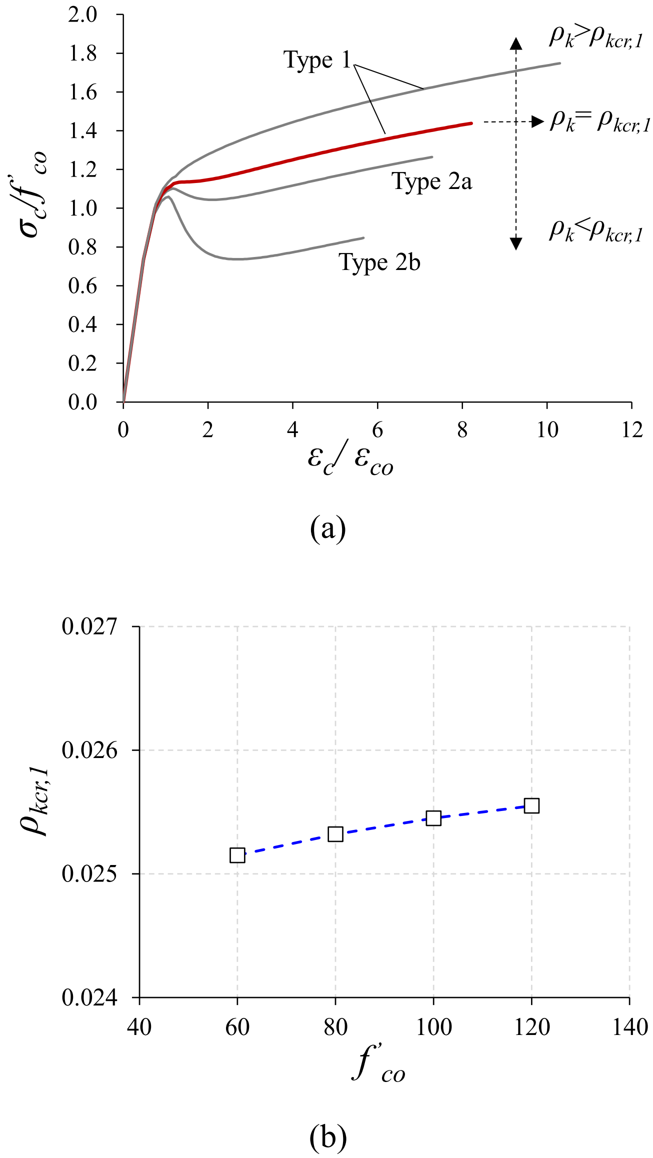

Fig. 15. Typical stress–strain behaviours of FRP confined HSC: (a) stress–strain curves; (b) critical confinement ratios for Type 1 behaviour.

equation for the subsequent analysis. Additionally, due to the large rupture strain of the PET FRP, the axial stress of the confined HSC can increase again after a sudden decrease of load at the first peak.

5. Stress–strain behaviours of FRP confined HSC

It is discussed by Yang and Feng [2] that the confinement ratio ρ_k represents the confining stiffness when the normalised coordinates are employed for analysis, and it is a key parameter for the confinement levels which determins the post-transition behaviour for the FRP confined concrete. Yang and Feng [2] provides critical values of ρ_k at the boundary of different confinement levels for NSC. For FRP confined HSC, there are two basic types of axial stress–strain behaviours: (i) Type 1: the axial stress keeps increasing with the axial strain until FRP ruptures; and (ii) Type 2: the axial stress experiences decreasing during the test. For Type 2 behaviours, there are two sub-classes, i.e., Type 2a: the axial stress is recoverable before FRP ruptures; and Type 2b: the axial stress is irrecoverable. The three types of stress–strain behaviours are shown in Fig. 15a. with the increase of ρ_k, the second portion of the stress–strain curves tilts up. The red curve with $\rho_k = \rho_{kcr,1}$ is the boundary of Type 1 and Type 2 behaviours, and the $\rho_{kcr,1}$ is denoted as the critical confinement ratio for Type 1 behaviour. When $\rho_k \geq \rho_{kcr,1}$, the specimen exhibits Type 1 behaviour. With the proposed model, the $\rho_{kcr,1}$ for HSC with 60 MPa$\leq f'_{co} \leq$ 120 MPa is solved numerically and plotted in Fig. 15b. The values for $\rho_{kcr,1}$ lie between 0.025 and 0.026. With the increase of f'_{co}, higher $\rho_{kcr,1}$ is necessary to achieve the Type 1 behaviour.

When $\rho_k < \rho_{kcr,1}$, the axial stress decreases after the first peak. At this moment, the lateral expansion of HSC is low and the confining stress provided by the FRP jacket is not fully activated. Due to the brittleness of HSC, the axial stress decreases. Meanwhile, the lateral expansion of HSC starts to accelerate and in turn leads to a rapid growth of confining

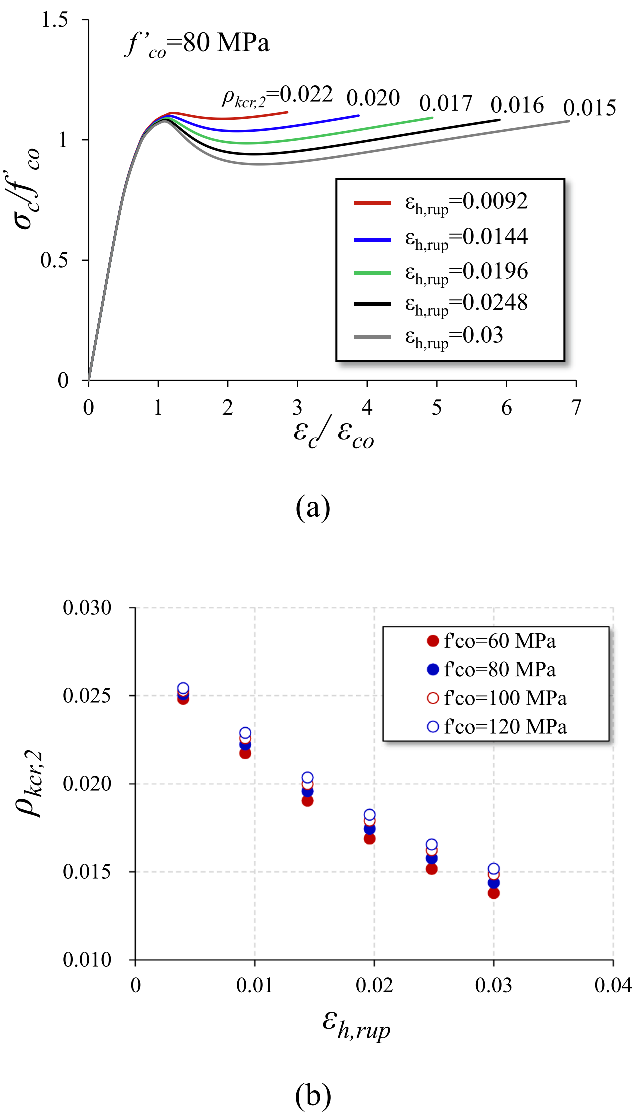

Fig. 16. Type 2 stress–strain behaviours of FRP confined HSC: (a) stress–strain curves; (b) critical confinement ratios for Type 2a behaviour.

stress. With the increase of axial strain and confining stress, the axial stress increases again. This type of behaviour is classified into Type 2. With sufficiently large rupture strain of FRP jacket ($\varepsilon_{h,rup}$), the axial strain of confined HSC will keep increasing and finally recover the first peak. However, due to the limitation of $\varepsilon_{h,rup}$, some of the specimen may fail before the stress recovery. Therefore, the Type 2a and Type 2b behaviours are determined by both ρ_k and $\varepsilon_{h,rup}$. A parametric study is conducted by varying $f_{co}^{'}$ and $\varepsilon_{h,rup}$. The range of $f_{co}^{'}$ is between 60 MPa and 120 MPa, and the $\varepsilon_{h,rup}$ is varied from 0.004 to 0.03, which covers typical CFRP, GFRP and AFRP materials (Lam and Teng [40]). Fig. 16a demonstrates the stress–strain curves of FRP confined HSC for$f_{co}^{'} = 80$ MPa. The presented curves are the critical cases that the stress recovery and $\varepsilon_{h,rup}$ are achived simutaneously. The ρ_k of these critical cases is denoted as the critical confinement ratio for Type 2a behaviour ($\rho_{kcr,2}$). When $\rho_{kcr,2} \le \rho_k \le \rho_{kcr,1}$, the specimen will have Type 2a behaviour. In order to achieve the stress recovery, the confined HSC with lower $\varepsilon_{h,rup}$ requires higher value of ρ_k, which is shown by Fig. 16b. For some special materials with $\varepsilon_{h,rup} < 0.004$ (e.g., high-modulus CFRP [40]), the calculated $\rho_{kcr,2}$ will be higher than $\rho_{kcr,1}$. This means for this kind of specimens, if $\rho_k < \rho_{kcr,1}$, it is impossible for the stress recovery and they will exhibit Type 2b behaviour. When $\rho_k \le \rho_{kcr,2}$, the FRP will rupture before the stress recovery, which is classified as Type 2b behaviour. Critical confinement ratios $\rho_{kcr,1}$ and $\rho_{kcr,2}$ are listed in Table 4. The readers can estimate the stress–strain behaviour of specific cases of FRP confined HSC by interpolating the values listed in the table.

6. Conclusions

In this study, the authors proposed a theoretical framework of analysis-oriented models for confined HSC incorporating path dependency. The proposed framework enables the model to identify the confining mode from the concrete state path without artificial intervention and can automatically select the proper behaviour for confined HSC with arbitrary loading paths. The key issues of the proposed model are concluded herein:

(i) Active 1st equation;
(ii) Damage initiation;
(iii) Reduction rules for the post-damaged 1st equation.

The proposed model achieves higher accuracy than existing path-dependent models in predicting the stress–strain behaviour of FRP confined HSC and performs well in modelling LRS FRP confined HSC. It should be noted that the mathematical forms and the corresponding parameters proposed by the authors are only employed herein to demonstrate the mechanism of path-dependent behaviour of confined HSC. The accuracy of this model is limited by the database used for model calibration. With more suitable mathematical forms and test databases, a better model can be built by addressing the three key issues of path dependency. Additionally, the methodology can be extended to other brittle materials with path-dependent behaviour, such as CAC [41–43], UHPC and rocks.

CRediT authorship contribution statement

Jia-Qi Yang: Conceptualization, Data curation, Formal analysis, Investigation, Methodology. **Peng Feng:** Conceptualization, Methodology, Resources, Funding acquisition, Project administration, Writing - review & editing, Supervision.

Declaration of Competing Interest

The authors declare that they have no known competing financial interests or personal relationships that could have appeared to influence the work reported in this paper.

Table 4
Critical confinement ratios.

f'_{co} (MPa)	$\rho_{kcr,1}$	$\rho_{kcr,2}$					
		$\varepsilon_{h,rup} = 0.004$	0.0092	0.0144	0.0196	0.0248	0.03
60	0.0252	0.0248	0.0217	0.0190	0.0169	0.0152	0.0138
80	0.0253	0.0251	0.0222	0.0196	0.0175	0.0158	0.0144
100	0.0255	0.0253	0.0226	0.0200	0.0179	0.0162	0.0149
120	0.0256	0.0254	0.0229	0.0204	0.0183	0.0166	0.0152

Acknowledgement

This work is supported by the National Natural Science Foundation of China (No. 51908322, 51978379 and 51678564), the Fundamental Research Funds for the Central Universities (No. 2021XJLJ01), China University of Mining and Technology (Beijing) Yue-Qi distinguished scholar award, and the research fund for the new faculty members provided by the School of Mechanics and Civil Engineering, China University of Mining and Technology (Beijing).

References

[1] Ozbakkaloglu T, Lim JC, Vincent T. FRP-confined concrete in circular sections: Review and assessment of stress–strain models. Eng Struct 2013;49:1068–88.
[2] Yang J-Q, Feng P. Analysis-oriented models for FRP-confined concrete: 3D interpretation and general methodology. Eng Struct 2020;216:110749. https://doi.org/10.1016/j.engstruct.2020.110749.
[3] http://thufeng.net/fcgjx/html/m03.html (accessed on 5/SEP/2021).
[4] Spoelstra MR, Monti G. FRP-confined concrete model. J Compos Constr ASCE 1999;3(3):143–50.
[5] Teng JG, Huang YL, Lam L, Ye LP. Theoretical model for fibre-reinforced polymer-confined concrete. J Compos Constr ASCE 2007;11:201–10.
[6] Lim JC, Ozbakkaloglu T. Investigation of the influence of the application path of confining pressure: tests on actively confined and FRP-confined concretes. J Struct Eng, ASCE 2015;141(8):04014203. https://doi.org/10.1061/(ASCE)ST.1943-541X.0001177.
[7] Han L-H, Hou C-C, Zhao X-L, Rasmussen KJR. Behaviour of high-strength concrete filled steel tubes under transverse impact loading. J Constr Steel Res 2014;92:25–39.
[8] Feng P, Cheng S, Bai Y, Ye L. Mechanical behaviour of concrete-filled square steel tube with FRP-confined concrete core subjected to axial compression. Compos Struct 2015;123:312–24.
[9] Hu HS, Xu L, Guo ZX, Shahrooz BM. Behaviour of eccentrically loaded square spiral-confined high-strength concrete-filled steel tube columns. Eng Struct 2020;216:110743.
[10] Ren FM, Liang YW, Ho JCM, Lai MH. Behaviour of FRP tube-concrete-encased steel composite columns. Compos Struct 2020;241:112139. https://doi.org/10.1016/j.compstruct.2020.112139.
[11] Xie J, Elwi AE, MacGregor JG. Mechanicao properties of three high-strength concretes containing silica fume. ACI Mater J 1995;92(2):135–45.
[12] Ansari F, Li Q. High-strength concrete subjected to triaxial compression. ACI Mater J 1998;95(6):747–55.
[13] Candappa DC, Sanjayan JG, Setunge S. Complete triaxial stress-strain curves of high-strength concrete. J Mater Civ Eng ASCE 2001;13(3):209–15.
[14] Lu X, Hsu C-T. Stress-Strain Relations of High-Strength Concrete under Triaxial Compression. J Mater Civ Eng ASCE 2007;19(3):261–8.
[15] Xiao QG, Teng JG, Yu T. Behaviour and modelling of confined high-strength concrete. J Compos Constr, ASCE 2010;14(3):249–59.
[16] Ho JCM, Ou XL, Chen MT, Wang Q, Lai MH. A path dependent constitutive model for CFFT column. Eng Struct 2020;210:110367. https://doi.org/10.1016/j.engstruct.2020.110367.
[17] Lai MH, Liang YW, Wang Q, Ren FM, Chen MT, Ho JCM. A stress-path dependent stress-strain model for FRP-confined concrete. Eng Struct 2020;203:109824. https://doi.org/10.1016/j.engstruct.2019.109824.
[18] Chen P, Wang Y, Liu C. Confinement path-dependent analytical model for FRP-confined concrete and concrete-filled steel tube subjected to axial compression. Compos Struct 2018;201:234–47.
[19] Lai MH, Song W, Ou XL, Chen MT, Wang Q, Ho JCM. A path dependent stress-strain model for concrete-filled-steel-tube column. Eng Struct 2020;211:110312. https://doi.org/10.1016/j.engstruct.2020.110312.
[20] Lim JC, Ozbakkaloglu T. Unified stress-strain model for FRP and actively confined normal-strength and high-strength concrete. J Compos Constr, ASCE 2015;19(4):04014072. https://doi.org/10.1061/(ASCE)CC.1943-5614.0000536.
[21] Chin C-L, Ma C-K, Awang AZ, Tan J-Y, Ong C-B, Omar W. Confining stress path dependent stress-strain model for pre-tensioned steel confined concrete. Eng Struct 2019;201:109769. https://doi.org/10.1016/j.engstruct.2019.109769.
[22] Lin S, Zhao Y-G, Lu Z-H. Modified confining stress path dependent analytical model for axially loaded circular normal, high and ultra-high strength concrete-filled steel tube stub columns. Compos Struct 2020;242:112192. https://doi.org/10.1016/j.compstruct.2020.112192.
[23] Jiang T, Teng JG. Analysis-oriented stress–strain models for FRP–confined concrete. Eng Struct 2007;29(11):2968–86.
[24] Lim JC, Ozbakkaloglu T. Confinement Model for FRP-Confined High-Strength Concrete. J Compos Constr, ASCE 2014;18(4):04013058. https://doi.org/10.1061/(ASCE)CC.1943-5614.0000376.
[25] Yu T, Teng JG, Wong YL, Dong SL. Finite element modelling of confined concrete-I: Drucker-Prager type plasticity model. Eng Struct 2010;32:665–79.
[26] Yu T, Teng JG, Wong YL, Dong SL. Finite element modelling of confined concrete-II: Plastic-damage model. Eng Struct 2010;32:680–91.
[27] Dai JG, Bai YL, Teng JG. Behaviour and Modelling of Concrete Confined with FRP Composites of Large Deformability. J Compos Constr, ASCE 2011;15(6):963–73.
[28] Bai YL, Dai JG, Teng JG. Cyclic Compressive Behaviour of Concrete Confined with Large Rupture Strain FRP Composites. J Compos Constr, ASCE 2014;18(1):04013025.
[29] Ye Y-Y, Liang S-D, Feng P, Zeng J-J. Recyclable LRS FRP composites for engineering structures: Current status and future opportunities. Compos B Eng 2021;212:108689. https://doi.org/10.1016/j.compositesb:2021.108689.
[30] Popovics S. Numerical approach to the complete stress-strain relation for concrete. Cem Concr Res 1973;3(5):583–99.
[31] Sargin M. Stress–strain relationship for concrete and the analysis of structural concrete section. Ontario, Canada: Univ. of Waterloo; 1971.
[32] Attard M, Setunge S. Stress–strain relationship of confined and unconfined concrete. ACI Mater J 1996;93(5):432–42.
[33] Kwan AKH, Dong CX, Ho JCM. Axial and lateral stress–strain model for FRP confined concrete. Eng Struct 2015;99:285–95.
[34] Dang Z, Feng P, Yang JQ, Zhang Q. Axial compressive behaviour of engineered cementitious composite confined by fibre-reinforced polymer. Compos Struct 2020;243:112191.
[35] Dong CX, Kwan AKH, Ho JCM. A constitutive model for predicting the lateral strain of confined concrete. Eng Struct 2015;91:155–66.
[36] Cui C, Sheikh SA. Experimental Study of Normal- and High-Strength Concrete Confined with Fibre-Reinforced Polymers. J Compos Constr, ASCE 2010;14(5):553–61.
[37] de Oliveira DS, Raiz V, Carrazedo R. Experimental study on normal-strength, high-strength and ultrahigh-strength concrete confined by carbon and glass FRP laminates. J Compos Constr, ASCE 2019;23(1):04018072. https://doi.org/10.1061/(ASCE)CC.1943-5614.0000912.
[38] Ozbakkaloglu T, Vincent T. Axial compressive behaviour of circular high-strength concrete-filled FRP Tubes. J Compos Constr, ASCE 2014;18(2):04013037.
[39] Zeng JJ, Ye YY, Gao WY, Smith ST, Guo YC. Stress-strain behavior of polyethylene terephthalate fibre-reinforced polymer-confined normal-, high- and ultra high-strength concrete. J Build Eng 2020;30:101243.
[40] Lam L, Teng JG. Design-oriented stress–strain model for FRP-confined concrete. Constr Build Mater 2003;17(6-7):471–89.
[41] Wang J, Feng P, Hao T, Yue Q. Axial compressive behaviour of seawater coral aggregate concrete-filled FRP tubes. Constr Build Mater 2017;147:272–85.
[42] Zhou W, Feng P, Lin H. Constitutive relations of coral aggregate concrete under uniaxial and triaxial compression. Constr Build Mater 2020;251:118957. https://doi.org/10.1016/j.conbuildmat.2020.118957.
[43] Zhou W, Feng P, Yang JQ. Advances in coral aggregate concrete and its combination with FRP: A state of- the-art review. Adv Struct Eng 2021;24(6):1161–81.